Global Biogeochemical Cycles

RESEARCH ARTICLE
10.1029/2020GB006571

Seasonal Carbon Dynamics in the Near-Global Ocean

L. Keppler[1,2], P. Landschützer[2], N. Gruber[3], S. K. Lauvset[4], and I. Stemmler[1]

[1]Max-Planck-Institute for Meteorology, Hamburg, Germany, [2]International Max Planck Research School on Earth System Modelling, Hamburg, Germany, [3]Environmental Physics, Institute of Biogeochemistry and Pollutant Dynamics, ETH Zurich, Zurich, Switzerland, [4]NORCE Norwegian Research Centre, Bjerknes Centre for Climate Research, Bergen, Norway

Key Points:
- We present a near-global monthly DIC climatology (MOBO-DIC) based on ship observations and a two-step neural network
- Seasonal surface DIC amplitudes range from 0 to more than 50 µmol kg^{-1}
- MOBO-DIC yields a spring-to-fall NCP in the euphotic zone of the mid-latitudes of 3.9 ± 2.7 Pg C yr^{-1}

Supporting Information:
- Supporting Information S1

Correspondence to:
L. Keppler,
lydia.keppler@mpimet.mpg.de

Citation:
Keppler, L., Landschützer, P., Gruber, N., Lauvset, S. K., & Stemmler, I. (2020). Seasonal carbon dynamics in the near-global ocean. *Global Biogeochemical Cycles*, *34*, e2020GB006571. https://doi.org/10.1029/2020GB006571

Received 7 FEB 2020
Accepted 22 NOV 2020
Accepted article online 6 DEC 2020

Abstract The seasonal cycle represents one of the largest signals of dissolved inorganic carbon (DIC) in the ocean, yet these seasonal variations are not well established at a global scale. Here, we present the Mapped Observation-Based Oceanic DIC (MOBO-DIC) product, a monthly DIC climatology developed based on the DIC measurements from GLODAPv2.2019 and a two-step neural network method to interpolate and map the measurements. MOBO-DIC extends from the surface down to 2,000 m and from 65°N to 65°S. We find the largest seasonal amplitudes of surface DIC in the northern high-latitude Pacific (~30 to >50 µmol kg^{-1}). Surface DIC maxima occur in hemispheric spring and minima in fall, driven by the input of DIC into the upper ocean by mixing during winter, and net community production (NCP) driven drawdown of DIC over summer. The seasonal pattern seen at the surface extends to a nodal depth of <50 m in the tropics and several hundred meters in the subtropics. Below the nodal depth, the seasonal cycle of DIC has the opposite phase, primarily owing to the seasonal accumulation of DIC stemming from the remineralization of sinking organic matter. The well-captured seasonal drawdown of DIC in the mid-latitudes (23° to 65°) allows us to estimate the spring-to-fall NCP in this region. We find a spatially relatively uniform spring-to-fall NCP of 1.9 ± 1.3 mol C m^{-2} yr^{-1}, which sums to 3.9 ± 2.7 Pg C yr^{-1} over this region. This corresponds to a global spring-to-fall NCP of 8.2 ± 5.6 Pg C yr^{-1}.

1. Introduction

The vast majority of the dissolved inorganic carbon (DIC) in the ocean is part of the natural carbon cycle. This pool of carbon amounts to approximately 38,000 Pg C (1 Pg C = 10^{15} g carbon), representing ~90% of the total amount of carbon in the ocean, atmosphere, and land biosphere system combined (Ciais et al., 2014). Since the beginning of the industrial revolution, human activities such as the burning of fossil fuels, land clearing, and the production of cement have released carbon dioxide (CO_2) into the atmosphere. The land and ocean carbon reservoirs respond to this perturbation by removing some of this additional, anthropogenic CO_2, thereby forming a negative feedback. As a result, the ocean DIC content had grown by 152 ± 20 Pg C in the Year 2007 relative to the Year 1800 (Gruber et al., 2019). The current oceanic net uptake rate of 2.5 ± 0.6 Pg C yr^{-1} constitutes approximately 23% of the annual anthropogenic CO_2 emissions, highlighting the crucial role of the ocean in ameliorating one of the key drivers of climate change (Friedlingstein et al., 2019). Thus, in the last four decades, studies investigating changes in the interior distribution of DIC have mainly focused on this long-term anthropogenic perturbation of oceanic DIC (Brewer, 1978; Chen & Millero, 1979; Gruber et al., 1996, 2019; Sabine et al., 2004; Sabine & Tanhua, 2010).

In contrast, variations in oceanic DIC occurring on seasonal timescales have received considerably less attention. This is a remarkable shortcoming, as the seasonal cycle represents one of the strongest signals of the natural carbon cycle in the ocean, and in most places, seasonal variations far exceed those occurring on interannual to decadal timescales (Bates, 2001; Bates et al., 2014; Brix et al., 2004; Dore et al., 2003; Gruber et al., 2002). Furthermore, changes in the seasonal cycle of DIC and other tightly linked carbonate system parameters, such as the surface ocean partial pressure of CO_2 (pCO_2) or oceanic pH, are predicted to occur in response to the oceanic uptake of anthropogenic CO_2 from the atmosphere (Hauck & Voelker, 2015; Kwiatkowski et al., 2018; Rodgers et al., 2008). These changes in the seasonal cycle can exacerbate the impact of ocean acidification on marine organisms, for example, through an earlier onset of a critical threshold (McNeil & Sasse, 2016). While changes in the seasonal cycle of surface pCO_2 have already been detected (Landschützer et al., 2018), no such studies of DIC exist. Subsequently, investigating the seasonal cycle of

DIC at present forms a crucial basis for investigating future changes in these patterns. The seasonal cycle of DIC is driven by the interaction of ocean circulation, vertical mixing, air-sea gas exchange, and net community production (NCP), that is, the net exchange of carbon between the inorganic and organic forms induced by the balance between photosynthesis and respiration/remineralization (Sarmiento & Gruber, 2006). Thus, provided that the contribution of the physical mechanisms can be estimated, the seasonal cycle of DIC in the water column can serve as an important quantitative constraint for biological productivity (Emerson et al., 2008; Gruber et al., 1998; Keeling et al., 2004; Ostle et al., 2015) and ultimately its response to a changing climate.

The earliest approaches to estimate NCP on a local level relied on oxygen measurements, which were then stoichiometrically related to changes in carbon to estimate NCP (Jenkins & Goldman, 1985; Riser & Johnson, 2008). Other studies have used measurements of nutrients or the isotopes of carbon or oxygen (Emerson et al., 2008; Gruber et al., 1998; Juranek et al., 2012; Plant et al., 2016; Quay & Stutsman, 2003) to infer NCP. However, such measurements are sparse, and thus, these studies remain limited to a few locations. Other studies used a combination of in situ and remotely sensed data to estimate the NCP statistically, but these studies had significant simplifications and assumptions that led to large uncertainties (Emerson, 2014; Li & Cassar, 2016). The only observation-based global mapped estimate of NCP to date was computed by Lee (2001), who used two methods to derive the seasonal cycle of surface DIC to then estimate NCP. One of their methods uses regional algorithms that estimate the surface DIC using surface temperature and nitrate as statistical predictors. Their second method estimates the surface DIC based on the ocean pCO_2 and total alkalinity, using thermodynamical models. These analyses resulted in a global estimate of the spring-to-fall NCP in the mixed layer of 6.7 ± 2.7 or 8.0 ± 2.7 Pg C yr^{-1}, depending on the method used. However, those estimates have large uncertainties as they are limited to surface data.

The long-term DIC observations from the subtropical time series (Bates et al., 2014; Dore et al., 2009), as well as oxygen observations from numerous locations, have demonstrated that the seasonal cycle seen at the surface extends, although with reduced amplitude, quite deep into the ocean interior. Additionally, one often finds a depth below which the phase of the seasonal cycle shifts by ~180°. Using seasonal oxygen data extending throughout the upper ocean, Najjar and Keeling (1997) investigated the depth where this shift in the seasonal cycle occurs on a global basis. They named this depth the oxygen nodal depth. This phase shift occurs because of the shifting balance between photosynthesis and mixing near the surface and respiration/remineralization below. A mapped monthly climatology of DIC across the water column would allow performing such an analysis for DIC.

A further reason to focus on the seasonal cycle of DIC is that it provides insights into the sensitivity of DIC to other perturbations, for example, those associated with climate change. It is a concern that the seasonal cycle of DIC and oceanic pCO_2 are not well captured in the current generation of Earth System Models used to make projections for the future behavior of the coupled carbon cycle climate system. For example, Mongwe et al. (2018) compared the CO_2 fluxes in 10 Earth System Models from the Coupled Model Intercomparison Project Phase 5 (CMIP5) in different sub-regions of the Southern Ocean. In these sub-regions, the models disagree on both the amplitude and phase of the seasonal cycle, and they disagree on the relative importance of DIC and temperature in regulating the seasonal air-sea CO_2 exchange. Additionally, how an Earth System Model represents the present-day seasonal cycle of DIC has been demonstrated to considerably affect the model's projected carbon uptake in the future (Nevison et al., 2016). Taken together, this illustrates the need to better constrain the seasonal cycle of DIC from observations and to better understand its drivers, in particular, the role of biological productivity. This will help to improve near-term predictions and longer-term projections of Earth System Models.

Due to data sparsity, establishing a global-scale analysis of the observation-based seasonal cycle of DIC in the water column is not straightforward (Figure 1). Across the global ocean, DIC measurements are currently primarily made as part of the repeat hydrographic program (Talley et al., 2016). These measurements provide a highly accurate basis to track the global-scale and long-term evolution of the oceanic carbon inventory, yet these measurements are sparse in space and time (Olsen et al., 2019; Talley et al., 2016). Important exceptions are the DIC measurements from various time series sites around the world, which permit detailed analyses of the seasonal cycle in the near-surface waters (Bates et al., 1996; Dore et al., 2003; Gruber et al., 1998, 2002; Keeling, 1993; Michaels et al., 1994). However, historically, there have only been seven stations with sufficient coverage to establish the climatological seasonal cycle without any form of statistical modeling

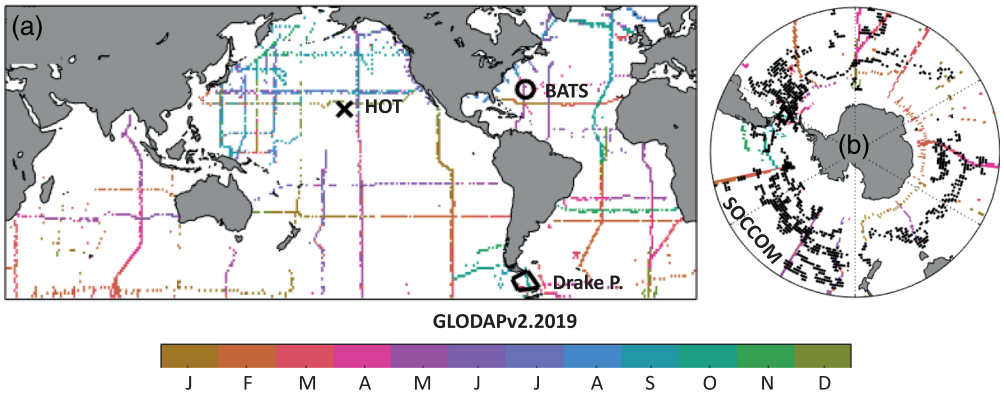

Figure 1. Map showing the locations of the DIC observations at 10 m from GLODAPv2.2019 from 2004 through 2017. Globally (a) and for the Southern Ocean (b). The months of the GLODAP measurements are shown in color. If a particular location was resampled, only the month of the last occupation is depicted. The location of independent validation data from the HOT, BATS, and Drake Passage time series stations (a) and SOCCOM floats (b) is marked in black.

(Bates et al., 2014). The measurements from these stations demonstrate that the phase and amplitude of the seasonal cycle of DIC vary considerably by location, but for the remainder of the ocean, the seasonal cycle of DIC remains poorly constrained.

In recent years, Argo floats equipped with biogeochemical sensors have complemented shipboard observations by measuring pH. These pH measurements can be used to calculate the DIC when combined with high-quality hydrography data and empirical algorithms (Bittig et al., 2018; Carter et al., 2018; Sauzède et al., 2017; van Heuven et al., 2011; Williams et al., 2017). Data assimilation efforts such as the Biogeochemical Southern Ocean State Estimate have begun to use these data to create a novel state estimate (Verdy & Mazloff, 2017); however, they are currently limited to the Southern Ocean.

An alternative means to establish the seasonal cycle of DIC at the global scale is to use a mapping method based on the available observations. This approach was taken by Sasse et al. (2013), who used a neural network method to produce global maps of surface DIC at seasonal resolution. More recently, Gregor and Gruber (2020) used an ensemble neural network method to map simultaneously surface alkalinity and pCO_2, from which they computed the variations in surface DIC. These artificial neural networks can map time-varying data based on complex, nonlinear relationships between the input and output data to overcome the existing challenges due to data sparsity (Dibike & Coulibaly, 2006; Hornik et al., 1989). While representing a major step forward, the previous work on mapping a DIC climatology by Sasse et al. (2013) and Gregor and Gruber (2020) is limited to the surface. For the ocean interior, the study by Lauvset et al. (2016) provides a measurement-based mapped DIC product extending over the entire upper ocean. However, their climatology is limited to the annual mean for a single reference year and is likely seasonally biased owing to the summer bias of the underlying DIC measurements. Recently, the first mapped monthly climatologies for alkalinity and DIC have been created for the global ocean based on ship measurements and a neural-network mapping technique (Broullón et al., 2019, 2020). While these studies highlight the importance of such data sets and the feasibility of neural network methods to create them, these studies rely on a single-step procedure and do not explore the potential of these data to solve long-standing questions such as the amount of carbon drawn down by biological activity.

Here, we deploy a method based on the two-step self-organizing maps, feed-forward networks (SOM-FFN) technique by Landschützer et al. (2013) to create a monthly climatology of Mapped Observation-Based Oceanic DIC (MOBO-DIC, Keppler et al., 2020) for the surface and interior ocean. Our novel data product is mapped on a 1° × 1° grid from 65°N to 65°S (i.e., near-global, hereafter global) on 33 depth levels between 2.5 and 1,975 m. We demonstrate that the resulting DIC fields adequately reproduce independent measurements from time series and biogeochemical float observations. Our monthly climatology provides information about the amplitude and phasing of the mean seasonal cycle of DIC at the surface and in the ocean's interior at a global scale. We use these data to determine the nodal depth and estimate the biological

carbon drawdown between hemispheric spring and fall, providing the first global estimation of spring-to-fall NCP from observation-based DIC estimates in the water column.

2. Data and Methods

2.1. SOM-FFN Mapping

We build on the SOM-FFN approach by Landschützer et al. (2013), in which the authors developed a two-step method to extrapolate sparse observations of the partial pressure of CO_2 (pCO_2) at the sea surface to the full global ocean domain. This two-step method belongs to a class of regression techniques as the mapping uses predictor data that are more frequently measured (Rödenbeck et al., 2015). In the first step of the SOM-FFN method, the data are clustered into regions using SOMs (Kohonen, 1989, 2001). This enables us to determine regional clusters of similar biogeochemical properties, particularly with regard to the seasonal cycle. In the second step, a FFN (Gardner & Dorling, 1998; Hagan et al., 2014) method is used in each of the clusters to determine the statistical relationship between pCO_2 and predictor data. These relationships are then applied in each cluster to map the surface pCO_2 to the global ocean.

We adapt that SOM-FFN approach using DIC as our target variable, different predictor data, and extending the mapping grid from three dimensions (latitude, longitude, and time) to four (latitude, longitude, depth, and time). Furthermore, we restrict the application to the mapping of a monthly climatology based on the monthly mean DIC from 2004 through 2017. Here, we provide a summary of our mapping approach and present the results from our validation tests. A more detailed description of the mapping technique and the validation tests we conducted with independent observations and synthetic data from biogeochemical model output can be found in supporting information Texts S1–S5.

We define our clusters (SOM-step) using globally mapped fields of climatological DIC and monthly climatologies of temperature and salinity. The latter two are taken from objectively interpolated monthly fields based on Argo float measurements from 2004 through 2017 (Argo, 2019; Roemmich & Gilson, 2009). The DIC is taken from the climatology by Lauvset et al. (2016), which does not resolve the seasonal cycle. We weight the DIC climatology with a factor of 3 so that the clusters, to a greater extent, represent regions of similar biogeochemical properties, and to a lesser extent, water masses defined by temperature and salinity. We tested different predictor variables and weights and found that clustering into six biogeochemical regions from the surface until 500 m, and four regions from 500 to 1,975 m, provides the best representation of the available observations. The resulting clusters highlight the zonal differences in physical and biogeochemical properties, as well as the differences in basins and within the water column (supporting information Figure S1).

For the FFN mapping, the choice of predictors is essential. Temperature and salinity are crucial candidate predictors as they control the solubility of CO_2 at the sea surface (Weiss, 1974) and the partitioning of DIC into the chemical species forming the DIC pool (Heinze et al., 2015; Takahashi et al., 2002). Temperature and salinity also characterize water masses and provide useful additional information about the transport and mixing of DIC. Nutrients and oxygen are also important candidates as predictor data (Sasse et al., 2013), as their distribution is strongly controlled by the biological carbon pump (Sarmiento & Gruber, 2006).

We decided to use temperature, salinity, dissolved oxygen, nitrate, and silicic acid as our set of predictors. We do not include phosphate or apparent oxygen utilization (AOU) as predictors because of the high correlation between nitrate and phosphate and dissolved oxygen and AOU in most regions. This choice is also based on our results indicating that the network does not improve further by including these predictors, while the degrees of freedom substantially increase. Similarly, we do not include information on the time or location as predictor data (e.g., latitude, longitude, depth, or month of the year). See supporting information Text S3 for a further discussion of our choices.

For the FFN, we use the same Argo-based temperature and salinity data set as employed for the SOM-step (Argo, 2019; Roemmich & Gilson, 2009) and take the monthly means at each grid cell from 2004 through 2017 again. We take monthly climatological values for dissolved oxygen, nitrate, and silicic acid from the World Ocean Atlas 2018 (WOA18; Garcia et al., 2019). These climatologies are based on observations gathered over the period from 1955 through 2017 and were mapped using an optimal interpolation technique.

As the Argo-based data set extends from 2.5 to 1,975 m, we use these depth levels as our minimum and maximum depths, respectively (Roemmich & Gilson, 2009). That data set starts in 2004; thus, we chose

2004 as the start year of the reference time period of our estimate. The dissolved oxygen fields from WOA18 extend from the surface down to 1,500 m and silicic acid and nitrate down to 500 m, only. Thus, we split the data into three vertical slabs (2.5–500, 600–1,500, and 1,600–1,975 m) and only use the predictors for the respective depth slabs where they are available, that is, temperature, salinity, dissolved oxygen, nitrate, and silicic acid from 2.5 to 500 m; temperature, salinity, dissolved oxygen, from 600 to 1,500 m, and temperature and salinity for the range from 1,600 to 1,975 m. We then interpolate all predictor data onto 33 uniform depth levels (supporting information Table S1).

The target data to be mapped are DIC ship measurements from the GLODAPv2.2019 data product by Olsen et al. (2019). We use the bottle data but retain only those with a WOCE quality control flag of 2 and a secondary GLODAP quality control flag of 1. We also retain only the DIC data from the period and grid points in which the Argo data product overlaps with the GLODAPv2.2019 data (2004 through 2017, 65°N to 65°S). The latter is intended to avoid inconsistencies between predictor and target data. Additionally, this use of a relatively restricted period also avoids potential issues with the long-term trend in DIC, primarily driven by the uptake of anthropogenic CO_2 by the ocean (Gruber et al., 2019). The final target data set comprises DIC measurements from 417 cruises (Figure 1). In the final preparation step, we linearly interpolate the data onto a regular $1° \times 1°$ grid and onto the same 33 depth levels as the predictor data (supporting information Table S1). The final data product (MOBO-DIC) extends from 65°N to 65°S, and from 2.5 to 1,975 m. Coastal regions are masked in our data product, as we do not have temperature and salinity available as predictor data there because the Argo floats mostly sample waters deeper than 2,000 m.

Several different types of uncertainties contribute to the total uncertainty of our DIC estimate. The first type of uncertainty is of random nature and is associated with how robustly our nonlinear regression approach is able to reproduce the observations that are used to train the network. To estimate this uncertainty, we apply a bootstrapping method (supporting information Text S2). The second type of uncertainty is of more structural nature, that is, how well our approach is able to fundamentally extrapolate the observations to the regions and times without observations. We assess this uncertainty using two approaches. First, we use independent observations from a few time series sites and biogeochemical Argo floats in the Southern Ocean. Second, we use synthetic observations from a model, reconstruct the model fields using our SOM-FFN approach, and then compare the reconstructed model fields with the actual model fields (supporting information Text S4).

As part of the bootstrapping method, we run our setup 10 times, where each time the network is run, a different subset of DIC data is randomly held-back to conduct an internal validation. We take the mean of the 10 runs as our best-guess output, and the standard deviation across the ensemble (hereafter ensemble spread) provides us with information on how robust our estimate is from one run to the next. This highlights the uncertainty within our method, which is expected to be higher in regions with fewer DIC observations. In most parts of the ocean, the ensemble spread is below 5 $\mu mol\ kg^{-1}$ (median, compared to typical values of DIC around 2,200 $\mu mol\ kg^{-1}$), but regionally, the spread is considerably higher (Figure 2). The northern Indian Ocean was very sparsely sampled during our analysis period, with no DIC observations at all in the Arabian Sea and only data from one cruise in the Bay of Bengal (see Figure 1). Thus, in the Northern Hemisphere Indian Ocean, our estimate is highly extrapolated and has a mean ensemble spread of 36 $\mu mol\ kg^{-1}$. In the Arabian Sea (north of the equator, between 40°E and 77°E), the spread is on average 45 $\mu mol\ kg^{-1}$, with up to 81 $\mu mol\ kg^{-1}$ at intermediate depth levels. Other regions that exhibit an ensemble spread that is above average are close to the surface in the North Pacific and the tropical Atlantic and Pacific Oceans. These regions are comparably well observed but have large variability near the surface (e.g., Feely et al., 2006). With the exception of the Arabian Sea, the ensemble spread becomes smaller in the deeper and seasonally less variable waters.

Next, we test our DIC estimate against independent observations from various locations around the globe, including time series stations in the subtropical northern latitudes (Hawaii Ocean time-series, HOT, Dore et al., 2009, and Bermuda Atlantic time-series Study, BATS, Bates et al., 2014) and repeat ship occupations (Drake Passage, Munro, Lovenduski, Takahashi, et al., 2015) and biogeochemical Argo floats (SOCCOM floats, https://soccom.princeton.edu/) in the Southern Hemisphere (supporting information Text S4). We find root-mean-square errors (RMSEs) ranging between 14 $\mu mol\ kg^{-1}$ at HOT and 30 $\mu mol\ kg^{-1}$ at Drake Passage. The mean biases range from $-16\ \mu mol\ kg^{-1}$ at locations co-located to SOCCOM floats to $+3\ \mu mol\ kg^{-1}$ at Drake Passage, where negative biases indicate that our estimate is on average lower than the validation data. Some of these differences can be attributed to differences from the substantial data extrapolation,

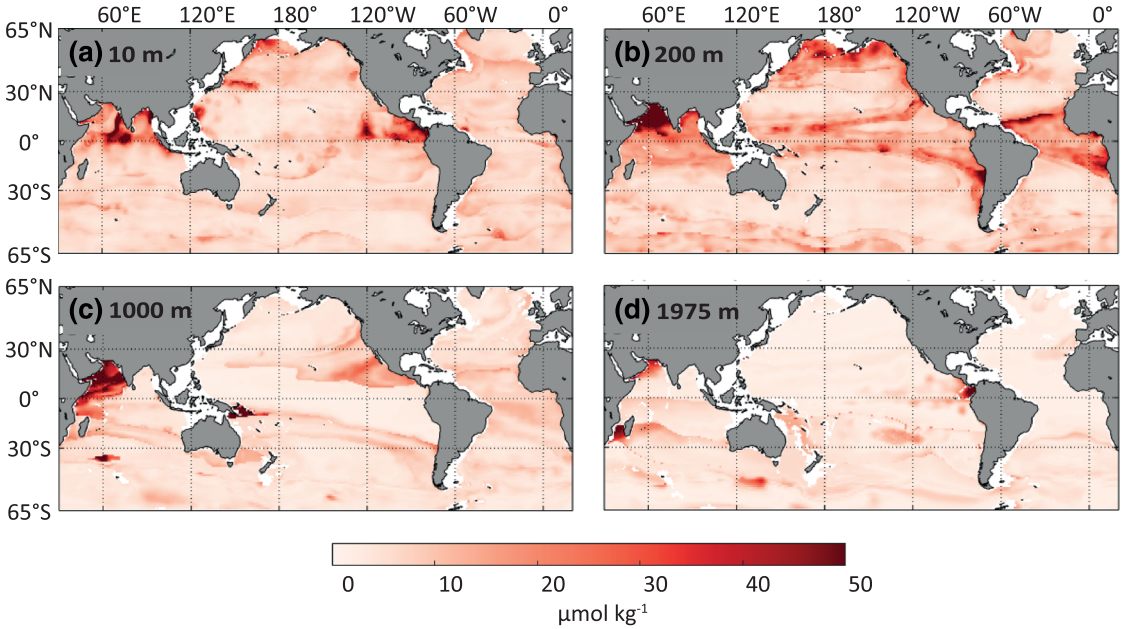

Figure 2. Maps of the ensemble spread of DIC on four depth levels: (a) 10, (b) 200, (c) 1,000, and (d) 1,975 m. The ensemble spread is the standard deviation of the estimates from a bootstrapping approach with 10 realizations. See text for more details.

highlighting the limits of our global approach to reconstruct the full spatiotemporal variability at single locations. Other differences stem from large interannual variability in the observations, rendering them not always representative of the climatological mean. In addition, there are known discrepancies between carbon measurements by ships and floats, explaining some of the differences between MOBO-DIC and the DIC calculated based on the measurements by SOCCOM floats (Bushinsky et al., 2019; Gray et al., 2018; Williams et al., 2017).

The synthetic data provide us an opportunity for further testing (supporting information Text S4). These synthetic data are created by sub-sampling the full model field of DIC from the ocean biogeochemical model HAMOCC (Ilyina et al., 2013; Mauritsen et al., 2019) at the time and location where we have DIC observations. We then run our method with these synthetic observations. We can then compare our reconstructed model fields with the model truth. Compared to the tests with independent observations, this test reveals a substantially smaller bias of +1 µmol kg^{-1} and an RMSE of 14 µmol kg^{-1}, indicating that some of the observed differences toward independent observations stem from the point-source nature, whereas our estimate comprises a 1° × 1° monthly average (an error often referred to as a representation error). There are some regions, such as the deep Indian and Pacific Oceans, where the RMSE is larger (up to 50 µmol kg^{-1}); these areas tend to be regions with few observations, where the ensemble spread illustrated in Figure 2 is also large. This highlights again that the regional uncertainties can be considerable using this approach. However, despite these regional uncertainties, the seasonal cycle of DIC is generally well represented in our reconstruction (supporting information Figure S6). For most of the global ocean, our reconstruction of the HAMOCC model fields is in phase with the model truth but underestimates the amplitude by up to 10 µmol kg^{-1}. This is consistent with findings for the sea surface pCO_2 from Landschützer et al. (2014), who found that the SOM-FFN method tends to underestimate the observed seasonal variability.

Given the sparsity of available measurements and the independent nature of the validation data, we argue that our SOM-FFN method passes important validation tests and can adequately map the monthly climatology of DIC at the global scale. A more extensive discussion of our validation tests, as well as a comparison with the climatology of DIC by Lauvset et al. (2016), can be found in supporting information Text S4.

2.2. Global DIC Inventory

To calculate the DIC inventory, we first use temperature and salinity fields from WOA18 (Garcia et al., 2019) to obtain spatially and temporally varying density fields to convert the DIC units from gravimetric (per kg) into volumetric (per m^3). We then spatially integrate the temporal mean of our volumetric DIC estimate.

To calculate the uncertainty of this estimate, we use the uncertainty of our data product based on the ensemble spread. For comparison, we additionally compute the DIC inventory using the climatology by Lauvset et al. (2016), first in the same domain as our study region (65°N to 65°S, until 2,000 m, with missing values in coastal regions), and then in the whole domain of the Lauvset climatology (extending until 5,500 m and including values at latitudes higher than 65°). Lastly, we upscale the DIC inventory based on the Lauvset climatology to estimate the total global DIC content in the ocean. We use the Lauvset climatology for this upscaling, as it covers considerably more ocean volume than our monthly climatology, and the temporal mean of our monthly climatology is comparable to the Lauvset climatology in the regions where the two estimates overlap. In addition to the mean DIC in the water column, we consider the volume of the grid cells containing DIC values in the Lauvset climatology and the global ocean volume of $1.335 \cdot 10^9$ km^3 (Amante & Eakins, 2009; Eakins & Sharman, 2010) to estimate the global DIC inventory. To calculate the uncertainty of the inventories using the Lauvset climatology, we use the uncertainty of that data product. In addition, for the global inventory, we use different realistic mean concentration scenarios in the regions that we upscale to provide us with a wide range, which we add to the uncertainty based on the Lauvset data. To estimate the range of the inventory in the unchartered regions, we use values between 1,950 and 2,300 µmol kg^{-1} in the coastal and high-latitude regions shallower than 1,000 m, 2,200 to 2,350 µmol kg^{-1} in the coastal and high-latitude regions deeper than 1,000 m, and values between 2,250 and 2,400 µmol kg^{-1} in the ocean deeper than 5,500 m. This wide range of scenarios is rather conservative, rendering us confident that the bounds straddle the true value of the global DIC inventory.

2.3. Nodal Depth and Spring-to-Fall NCP

To investigate the effect of biological activity on the seasonal cycle of DIC, we first compute the DIC nodal depth. Above and below that depth, the phase of the seasonal cycle of DIC differs due to the opposing effects of primary production and mixing near the surface and respiration/remineralization below. We determine the nodal depth as the depth where the amplitude of the seasonal cycle of DIC is minimal, while it increases both upward and downward of the nodal depth.

To help us interpret the nodal depth, we compare it to the deepest mixed layer depth (MLD) in hemispheric winter and the annual-mean depth of the euphotic zone. We compute the maximum winter MLD using the Argo-based MLD product by Holte et al. (2017) and use an optimal interpolation to fill the gaps. We then only consider the months between hemispheric fall and spring, where spring starts in April or October and fall starts in October and April, in the Northern and Southern Hemispheres, respectively. We calculate the depth of the euphotic zone (z_{eu}) on the basis of the 1% light level criterion using SeaWiFS chlorophyll-a data from the National Aeronautics and Space Administration (NASA) ocean color website (https://oceancolor.gsfc.nasa.gov/cgi/l3?sen=S&per=MO&prod=CHL_chlor_a), following Morel et al. (2007) (Equation 1).

$$log_{10} z_{eu} = 1.524 - 0.460 \cdot X - 0.00051 \cdot X^2 + 0.0282 \cdot X^3 (X = log_{10}[Chl]_{surf}), \quad (1)$$

with $[Chl]_{surf}$ given in units of mg m^{-3}.

To determine the spring-to-fall NCP, that is, the biological drawdown of DIC between hemispheric spring and fall at each grid point, we solve the DIC balance of the euphotic zone (between the surface and z_{eu}) for NCP (cf. Gruber et al., 1998) (Equation 2). In this balance, we are considering, next to NCP, the contribution of air-sea gas exchange, vertical diffusion, and vertical entrainment. This means that we are neglecting the contribution of the horizontal divergence of the horizontal transport, primarily because it is not straightforward to estimate this component based on observations alone. Furthermore, in many regions, this contribution is relatively small, although there are notable exceptions, such as in the Southern Ocean and at the equatorial western boundaries (Talley et al., 2011), adding to the uncertainty of our estimate.

With these considerations, the time- and depth-integrated DIC balance equation reads

$$\int_{t=ts}^{t=tf} \int_{z=-z_{eu}}^{z=0} NCP dz dt = -\int_{t=ts}^{t=tf} \int_{z=-z_{eu}}^{z=0} \frac{dDIC_s}{dt} dz dt - \int_{t=ts}^{t=tf} F_{air.sea} dt + \int_{t=ts}^{t=tf} F_{diff} dt + \int_{t=ts}^{t=tf} F_{entr} dt, \quad (2)$$

where NCP is the instantaneous NCP, $\frac{dDIC_s}{dt}$ is the time rate of change of the salinity-normalized DIC (normalized using the annual mean salinity at each grid cell as reference salinity), $F_{air.sea}$ is the air-sea CO_2 flux, F_{diff} is the vertical diffusive flux, and F_{entr} is the entrainment flux, that is, the flux that occurs when the

mixed layer is deeper than the euphotic zone and deepens from 1 month to the next. All quantities are integrated over the hemispheric summer, that is, from spring (*ts*) to fall (*tf*,) where we take the months of April for spring and October for fall in the Northern Hemisphere and vice versa in the Southern Hemisphere.

For the following calculations, unless otherwise stated, we use monthly climatologies determined over the period from 2004 through 2017 on a $1° \times 1°$ grid. We use the mean z_{eu} between hemispheric spring and fall; that is, we keep it constant in time.

The DIC time rate of change term (first term on the right-hand side of Equation 2) is determined from our climatology by first converting the gravimetric DIC concentration to volumetric concentration, using the temporally and spatially varying density obtained from the Argo climatology (Roemmich & Gilson, 2009), then normalizing the DIC for salinity, also using the temporally and spatially varying Argo salinity, and finally integrating in depth and time. As we keep z_{eu} constant, this term thus simplifies to $\int_{z=-z_{eu}} z = 0\,(DIC(tf) - DIC(ts))\,dz$. For the air-sea flux term, that is, the second term of Equation 2, we use the updated air-sea CO_2 product by Landschützer et al. (2014) based on its latest extension in time (v2018, updated until December 2017), as presented in Keppler and Landschützer (2019). We estimate the diffusion term (i.e., the third term of Equation 2) following Fick's first law in Equation 3:

$$F_{diff} = -k_z \frac{dDIC_s}{dz}\,(at\,z = -z_{eu}), \tag{3}$$

where k_z is the diffusivity coefficient and where $\frac{dDIC_s}{dz}$ is the vertical gradient of our salinity-normalized DIC at the base of the euphotic zone. For k_z, we use a constant value of $1.3 \cdot 10^{-5}\ m^2\ s^{-1}$), which is representative for the diffusivity in the thermocline in regions of intermediate winds (Denman & Gargett, 1983; Dillon & Caldwell, 1980), in-line with recent estimates by Whalen et al. (2012). The entrainment term (i.e., the fourth term of Equation 2) is considered only when the mixed layer is deeper than the euphotic zone and when it deepens from one month to the next. We estimate it using Equations 4 and 5:

$$F_{entr.ML} = -\frac{dh}{dt}\frac{dDIC_s}{dz}\,(at\,z = -h), \tag{4}$$

where $F_{entr.ML}$ is the entrainment flux into the mixed layer, h is the MLD, and $\frac{dh}{dt}$ is the entrainment rate, that is, how fast the MLD deepens over one month. We use the monthly climatology of the MLD by Holte et al. (2017) and apply an optimal interpolation to fill observational gaps and compute the mean MLD over hemispheric summer. As not all of the entrained water enters the euphotic zone, we compute the part of the entrained water into the euphotic zone using Equation 5, assuming that the entrained water has evenly mixed within the mixed layer from one month to the next:

$$F_{entr} = \frac{F_{entr.ML}}{h} z_{eu} \tag{5}$$

We limit our estimation of NCP to the spring-to-fall period since the calculation of NCP during the winter months is fraught with large uncertainty. First, NCP is much smaller in winter, and sometimes even negative. Second, the physical contributions from mixing and transport tend to be much larger, thereby dominating the budget. As a result, NCP would emerge as a small residual of much larger terms, making this estimate highly uncertain. Thus, we only calculate the spring-to-fall NCP, where we are confident the method is robust within the uncertainty range.

We calculate the uncertainty of our NCP estimate (U_{NCP}) by adding the individual uncertainties (Equation 6):

$$U_{NCP} = e_1 + e_2 + e_3, \tag{6}$$

with this error propagation choice reflecting a more conservative approach compared to the more common Gaussian model where the squared errors are added, and then the square root of the sum is taken.

The first error, that is, e_1, is the uncertainty associated with estimating the difference in DIC between spring and fall. We estimate this error using our tests with the synthetic data (see supporting information Text S7). There, we find that the estimated spring-to-fall NCP in the mid-latitudes (23° to 65°) using DIC from the output of the ocean biogeochemistry model HAMOCC tends to spread substantially across the ensemble

members of the bootstrapping approach and also tends to be biased high. While the model truth suggests a spring-to-fall NCP of 1.5 Pg C yr^{-1}, the reconstruction based on the synthetic data suggests an NCP ranging from 1.9 through 2.4 Pg C yr^{-1}. Rather than developing a detailed error attribution, we take a more conservative approach and propagate the largest difference as our upper uncertainty bound. The largest discrepancy between a member (2.4 Pg C yr^{-1}) and the model truth (1.5 Pg C yr^{-1}) thus yields an uncertainty of 60%.

The second error, that is, e_2, is the error due to the uncertainty of the mapped air-sea CO_2 fluxes by Landschützer et al. (2013). That error has been recently estimated to be 17% (Roobaert et al., 2019). To translate e_2 to the NCP uncertainty, we run a sensitivity analysis, where we calculate the NCP with air-sea CO_2 fluxes 17% lower and then with 17% higher than the mean fluxes. From that, we derive an uncertainty of 5% in the final NCP uncertainty.

Lastly, the third error, e_3, encapsulates the uncertainty of the diffusive flux. In the absence of a mapped global time-varying product of the diffusivity coefficient k_z, we use a constant k_z, which is representative of the thermocline in regions of intermediate wind strength (Denman & Gargett, 1983; Dillon & Caldwell, 1980). As k_z does vary substantially in time and space, the constant value of k_z adds regional uncertainty to our NCP estimate (Whalen et al., 2012). To quantify e_3, we run a sensitivity test, where we estimate the spring-to-fall NCP with higher and lower diffusivity coefficients, which are representative for the thermocline for regions of weak and strong winds ($4.1 \cdot 10^{-6}$ and $2.0 \cdot 10^{-5}$ m^2 s^{-1}, respectively Denman & Gargett, 1983; Dillon & Caldwell, 1980). From that analysis, we obtain an uncertainty of 3%.

We do not add error estimates from F_{entr} as we lack a mechanistic understanding of the uncertainties and also because its contribution to the overall NCP is minor compared to the other terms we considered. In addition, we had to neglect the horizontal transport divergence. This adds further uncertainty, which we cannot quantify here. However, our chosen approach to calculate the total uncertainty of the NCP (Equation 6) is conservative compared to the common approach of using the square root of the sums of the squared errors, giving us confidence in our uncertainty range. Solving Equation 6 with e_1 to e_3, we obtain a total NCP uncertainty of 68%, which is mostly due to the uncertainty in our MOBO-DIC estimate of the spring-to-fall DIC drawdown.

3. Results and Discussion

3.1. DIC Distribution

Our reconstructed climatology of ocean interior DIC (MOBO-DIC) portrays the well-known large-scale DIC distribution (Figures 3a–3d and 4). We find the lowest DIC concentrations near the ocean surface, a strong increase of DIC with depth, and a large-scale increase in DIC below 1,000 m along the large-scale overturning circulation from the Atlantic to the Pacific.

In the global average, the DIC increases from a concentration of ~2,044 ± 69 μmol kg^{-1} at 2.5 m to ~2,270 ± 68 μmol kg^{-1} at 1,975 m. This vertical DIC gradient is known to be due to the ocean carbon pumps, that is, global gradient makers that maintain these differences against ocean mixing (Gruber & Sarmiento, 2002). These pumps include the (mostly) vertically acting biological pumps (soft-tissue and $CaCO_3$ pumps) (Boyd, 2019) and the more laterally acting solubility pump that brings cold, DIC-rich waters from the high latitudes to depth. Superimposed on that is the large-scale overturning circulation, which leads to an accumulation of DIC stemming from the remineralization (soft-tissue pump) or dissolution ($CaCO_3$ pump) of the sinking matter associated with the biological pumps. As a result, there is a distinct gradient of DIC from the younger water (i.e., water that has been out of contact with the atmosphere for short periods) in the Atlantic to the older waters of the Pacific along the global-scale flow associated with the overturning circulation (Heinze et al., 2015).

Spatial features near the surface include a distinct latitudinal gradient, with surface ocean DIC increasing, in the zonal average, from ~1,985 μmol kg^{-1} at the equator to ~2,166 μmol kg^{-1} at 65°N/S (Figure 3a). This gradient is driven primarily by temperature and upwelling (Wu et al., 2019) but modified by the degree to which the air-sea CO_2 flux eliminates any air-sea CO_2 disequilibria (Sarmiento & Gruber, 2006). Variations in the buffer factor, which is primarily controlled by alkalinity and indirectly by temperature, also modify the gradient (Sarmiento & Gruber, 2006). At the surface, net freshwater fluxes affect DIC also quite considerably through a dilution/concentration effect, with regions of excess rainfall over evaporation, that is, regions with generally low salinity having lower DIC, and vice versa. This explains the generally lower DIC

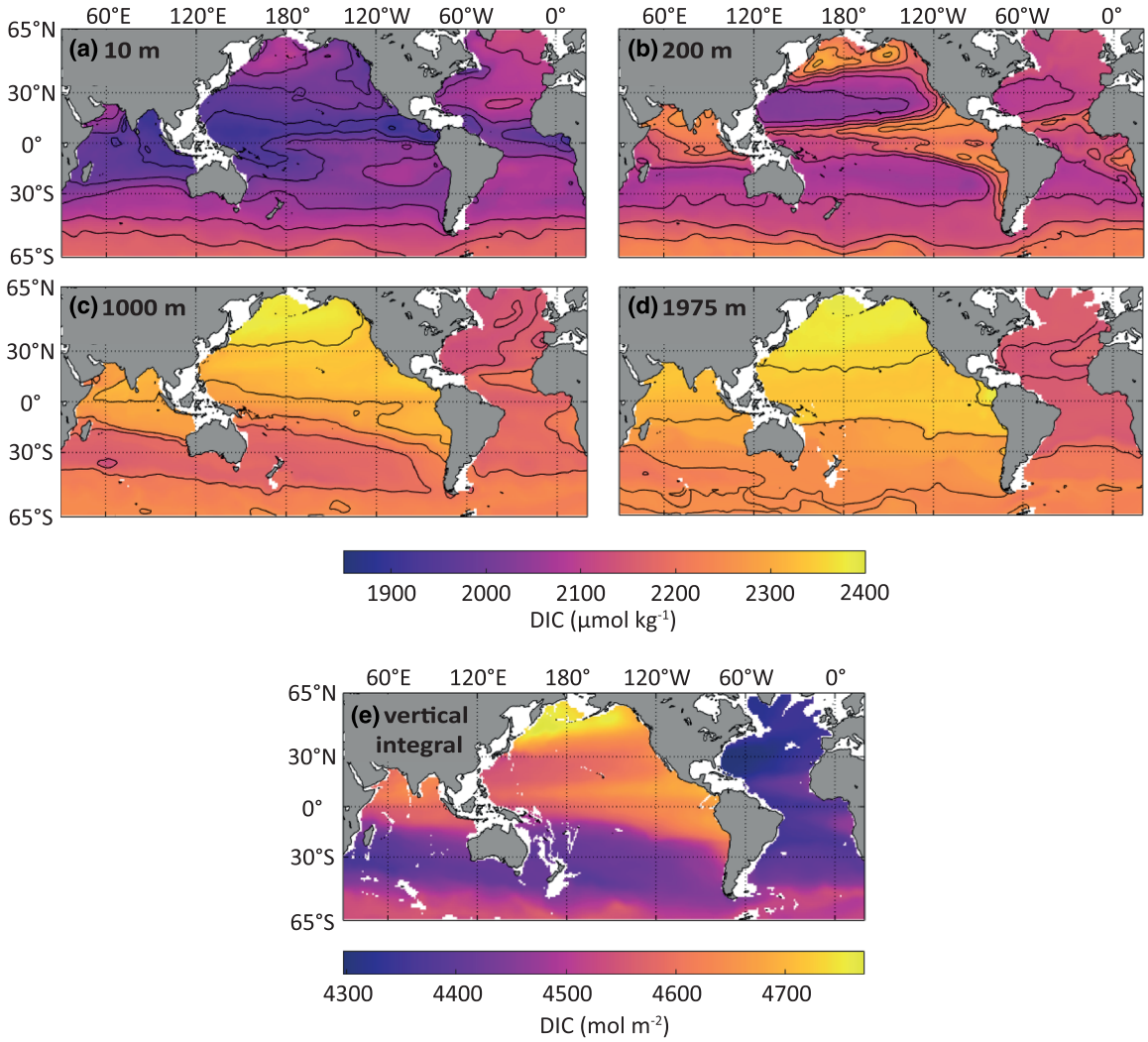

Figure 3. Maps of the annual mean DIC concentration in MOBO-DIC on four depth levels: (a) 10, (b) 200, (c) 1,000, and (d) 1,975 m. Black contour lines are drawn every 50 µmol kg^{-1}. (e) Map of the vertically integrated DIC between 2.5 and 1,975 m, excluding areas shallower than 1,975 m.

concentrations in the Pacific versus those in the Atlantic. It also explains the unusually low DIC values north of the equator in the eastern Tropical Pacific, a region with a strong excess of rainfall, and hence very low salinity.

At 200 m depth, the DIC distribution is primarily governed by the contrast between the gyres and the shadow zones in the eastern part of the basins (Figure 3b). The low ventilation of waters in these shadow zones tends to accumulate the DIC stemming from the remineralization of the exported organic matter. At the same time, these zones tend to have low to very low oxygen concentrations, leading to the high CO_2, low oxygen zones described by Paulmier et al. (2011).

In the intermediate waters (~500 to ~1,500 m), the distribution of DIC becomes more uniform (Figure 3c). Exceptions are the deep-water formation regions such as the North Atlantic and the Southern Ocean, which have lower DIC concentrations than most other regions at these depths, reflecting the relatively young waters. In the deep ocean (below ~1,500 m), the DIC concentration is the highest with a mean of ~2,300 µmol kg^{-1} (Figure 3d). The deep waters in the North Pacific are the oldest; that is, they have been out of contact with the atmosphere for ~1,500 yr. Thus, the largest amounts of DIC are stored here, with a mean DIC concentration of ~2,400 µmol kg^{-1} at 1,975 m (Heinze et al., 2015; Sarmiento & Gruber, 2006).

The column inventory of annual mean DIC, obtained by integrating at each grid point the DIC concentration vertically from the surface down to 1,975 m, largely reflects the changes in the deep ocean, that is,

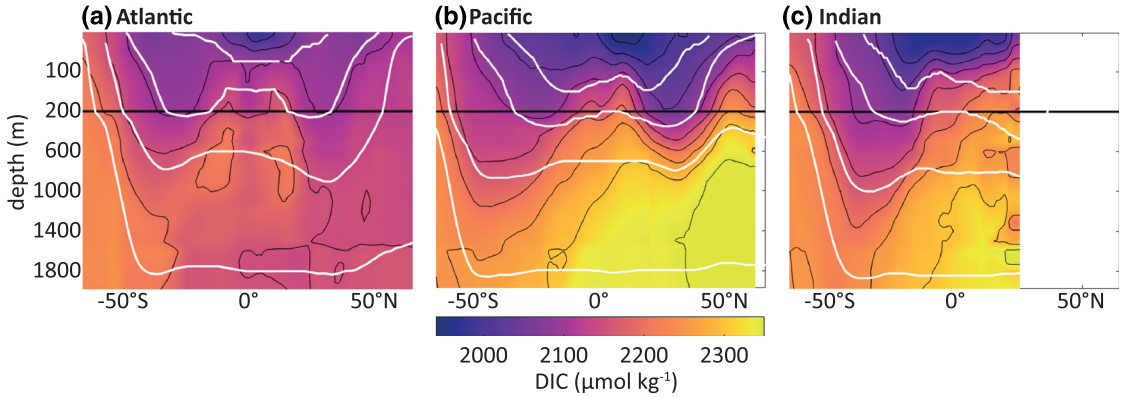

Figure 4. Vertical zonal sections of the annual mean DIC. Shown are the zonal means of DIC for the Atlantic (a), Pacific (b), and Indian (c) Oceans. Zoomed into the top 200 m (delimited in black); key isopycnals as illustrated as white lines (from top to bottom: 24.5, 26.2, 27.6, and 28.4 kg m^{-3}); black contour lines are drawn every 50 µmol kg^{-1}.

the accumulation of DIC from the Atlantic to the Pacific (Figure 3e). Consequently, the highest column inventories are found in the North Pacific and the lowest in the North Atlantic. Superimposed on this global-scale gradient are elevated inventories in the eastern parts of the ocean basins, reflecting the high DIC concentrations in the oxygen minimum zones.

The MOBO-DIC climatology yields a DIC inventory of 15,500 ± 210 Pg C over the domain covered by this product, that is, from 65°N to 65°S, and from 2.5 to 1,975 m in all water bodies with a bathymetry deeper than 1,975 m (see Figure 3e). This value is very similar to the value we obtain from the Lauvset climatology if we integrate it over the same grid cells. The difference between the two climatologies amounts to only 70 Pg C (~0.4%), which is remarkable given the large differences in how these two climatologies were inferred from the observations.

For reference, we also calculate the DIC inventory for the whole domain of the Lauvset climatology, which extends down to 5,500 m and includes values in coastal waters and marginal seas, as well as at latitudes higher than 65°, thus covering ~92% of the ocean volume. Over that domain, the Lauvset climatology yields a DIC inventory of ~34,300 Pg C (34,283 ± 98) Pg C. Making use of the known ocean volume in addition to a range of scenarios of different possible DIC concentrations in the unchartered waters (see section 2), we upscale the DIC inventory to obtain the total DIC contained in the global oceans. This upscaling yields a total DIC inventory of ~37,200 Pg C (37,214 ± 195 Pg C), which is substantially lower than the DIC inventory of 38,000 Pg C that has been used in most global carbon budgets (e.g., Friedlingstein et al., 2019; Le Quéré et al., 2018; Sarmiento & Gruber, 2002) and in most assessments by the Intergovernmental Panel on Climate Change (IPCC) to date (Ciais et al., 2014). This 38,000 Pg C estimate has been perpetuated in the literature, at least since the IPCC's third assessment report (Prentice et al., 2001). However, the origin of the 38,000 Pg C inventory estimate is not entirely clear, but it builds on the 39,000 Pg C estimate that was established in 1985 by Sundquist (1985) and was later used by Siegenthaler and Sarmiento (1993). Sundquist based his inventory on the data collected during the 1970s by GEOSECS. Thus, the community has been relying on an ocean DIC inventory estimate that was established more than 30 years ago based on extraordinary sparse data. The improvements in sampling and data analysis since then suggest that it is time to update the 38,000 Pg C estimate and use our new estimate of 37,200 ± 200 Pg C instead.

3.2. Seasonal Cycle of Surface DIC

In fall and winter, entrainment by deepening mixed layers injects a substantial amount of DIC from the upper thermocline into the surface ocean, resulting in surface DIC reaching its seasonal maximum in winter. In contrast, over the spring and summer months, when light availability is highest, biological productivity removes considerable amounts of inorganic carbon from the DIC pool, resulting in the seasonal minimum to occur in late summer. Figure 5 highlights this seasonal drawdown of DIC between hemispheric spring and fall. Integrated over the upper 100 m, the DIC drawdowns amount, on average, to 2 mol m^{-2} yr^{-1} in the mid-latitudes (23° to 65°). Some of the largest reductions with values of more than 4 mol m^{-2} yr^{-1} are found in the northwestern Pacific. Conversely, the seasonal reduction of DIC is generally less than 1 mol m^{-2} yr^{-1} in the higher latitudes of the Southern Hemisphere. In addition, there are patches in the tropics, where the

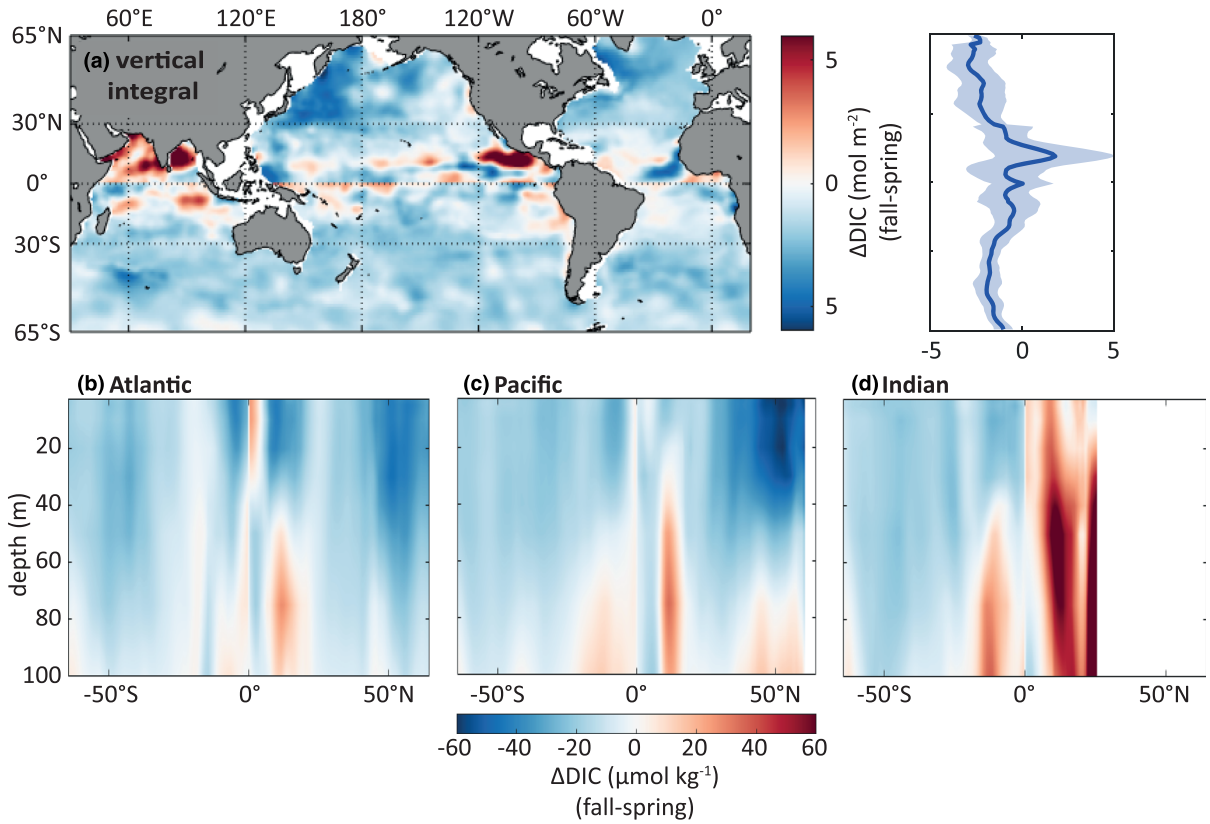

Figure 5. Analyses of the changes in DIC between hemispheric spring and fall. (a) Map of the change in vertically integrated DIC in the upper 100 m between hemispheric spring and fall; side panel: zonal mean ±1 standard deviation. (b–d) Vertical sections of the zonally averaged changes in DIC in the upper 100 m from hemispheric spring to fall for the (b) Atlantic, (c) Pacific, and (d) Indian Oceans.

DIC in the upper 100 m increases between hemispheric spring and fall, reflecting the very small seasonal cycle with seasons that are not simply aligned with the extra-tropical seasons (owing, e.g., to the seasonal reversal of the monsoon system in the Indian Ocean Sarma et al., 2013).

The vertical sections in Figures 5b–5d demonstrate that the majority of the decrease occurs in the upper 50 m, with the signal getting weaker with depth. In some places, the signal even reverses its sign. Here respiration/remineralization at depth seems to dominate over the uptake of carbon through photosynthesis near the surface. In sections 3.3 and 3.4, we further investigate the change in DIC with depth linked to the shift in dominance of processes near the surface and below, as well as the biological drawdown of DIC between hemispheric spring and fall (i.e., the spring-to-fall NCP).

The phase and amplitude of the surface seasonal cycle of DIC are shown in more detail in Figures 6, 7b, and 7c. The strong similarity of the seasonal cycles of DIC (Figures 6a and 6c) and salinity normalized DIC (Figures 6b and 6d) suggests that the seasonal variations in the net freshwater fluxes have, at least on a large scale, little influence on the seasonal variations in DIC. Unsurprisingly, the mean phase is 6 months out of phase in the two hemispheres, with the highest surface DIC concentrations occurring in early spring when vertical mixed layers tend to be deepest (Holte et al., 2017) and deep mixing brings DIC-rich waters to the surface. Conversely, the surface DIC is lowest in early fall, in response to increased biological drawdown of DIC during summer. However, the phase of the seasonal cycle varies regionally and with the onset of local phytoplankton blooms. Another interesting feature is that the phase of the seasonal cycle of DIC in the northern Indian Ocean is similar to that in the Southern Hemisphere, likely owing to the strong reversal of the monsoon circulation in this region (Sarma et al., 2013). At the same time, we note that due to the extremely sparse DIC observations in this region and the associated large uncertainties (Figure 2), this feature could be an artifact.

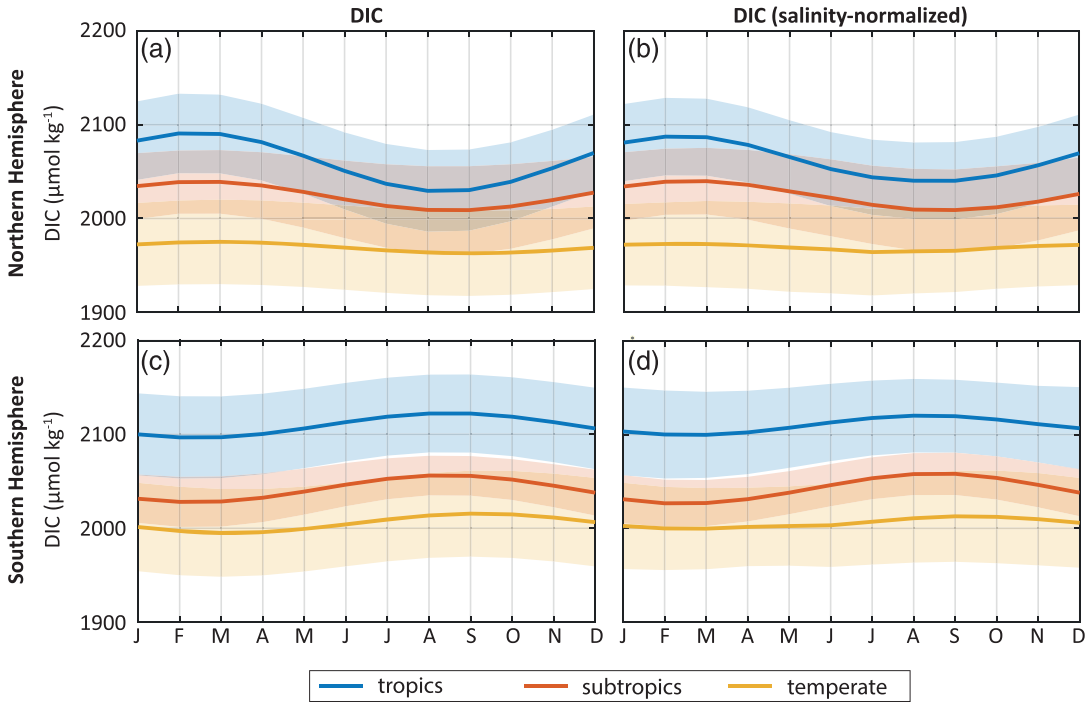

Figure 6. Time series of the climatological mean seasonal cycles of DIC (a and c) and salinity normalized DIC (b and c) in the surface ocean (at 2.5 m) in different climate regions. Temperate (35° to 65°, blue), subtropical (23° to 35°, orange), and tropical (0° to 23°, yellow) for the Northern (a and b) and Southern (c and d) Hemispheres. The solid lines indicate the mean and the shading the range spanned by the standard deviation within that region. The boundaries for the climate regions are illustrated on the map grid in Figure 7a. For the salinity normalization, the local annual mean salinity was used.

For most of the ocean, the amplitude of the seasonal cycle of surface DIC (measured here as half of the seasonal maximum minus the seasonal minimum) ranges between 5 and 20 µmol kg^{-1} with a median value of 14 µmol kg^{-1} (Figures 6 and 7a), but there are substantial regional differences. The largest amplitudes are found in the high-latitude North Pacific with amplitudes exceeding 50 µmol kg^{-1}. The high-latitude North Atlantic also exhibits large amplitudes with values ranging between 30 and 50 µmol kg^{-1}. These large amplitudes are the consequence of strong seasonal forcing from the atmosphere with deep mixing in the winter (Holte et al., 2017; Lozovatsky et al., 2008), strong stratification in summer, and a distinct seasonal cycle in biological activity. These larger amplitudes also extend into the temperate regions, especially in the Northern Hemisphere, with typical amplitudes of ~32 µmol kg^{-1}. Weaker amplitudes are found in the subtropical regions with values of ~15 µmol kg^{-1} and the weakest ones in the tropical regions (~8 µmol kg^{-1}), where the seasonal atmospheric forcing is minimal.

The distinct latitudinal pattern observed in the extra-tropical latitudes of the Northern Hemisphere is not found in the corresponding latitudes of the Southern Hemisphere. Here, the amplitude remains relatively small throughout the extra-tropics. A plausible explanation is that persistent upwelling in combination with a weaker biological activity due to iron limitation (Gervais et al., 2002) dampens the seasonal DIC cycle in austral spring/summer, particularly in the Southern Ocean south of 35°S. However, we also need to recognize that our method may underestimate the seasonal cycle in the Southern Ocean (see supporting information Text S4.4).

While we identify some clear large-scale patterns of the amplitude of the seasonal cycle, these patterns remain patchy in places. In particular, the seasonality of the tropical Pacific and tropical Atlantic may be obscured by large interannual variability linked to tropical modes such as the El Niño–Southern Oscillation (Feely et al., 2006). Furthermore, as illustrated in Figure 2, we have less confidence in smaller-scale features given the elevated ensemble spread at smaller scales.

3.3. Nodal Depth

Similar to the oxygen nodal depth described by Najjar and Keeling (1997), we find a change in the phase of the seasonal cycle of DIC with increasing depth. This is well illustrated by the MOBO-DIC data from

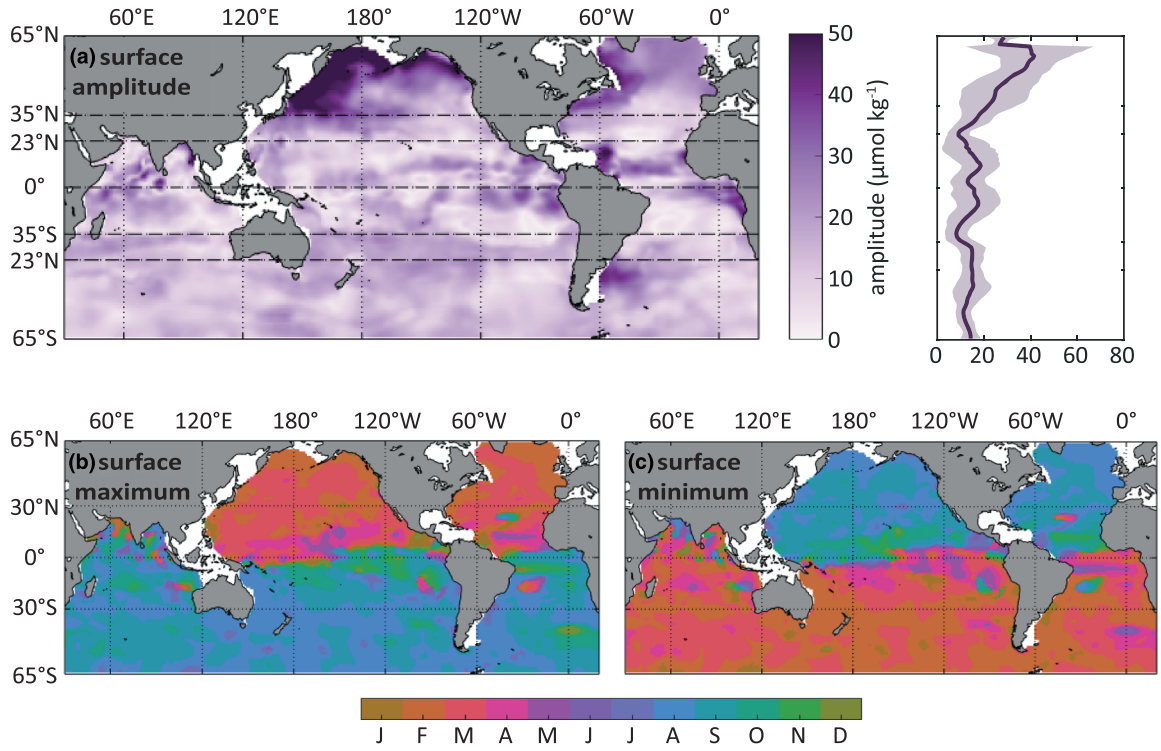

Figure 7. Maps illustrating the amplitude and phase of the climatological seasonal cycle of surface ocean DIC (at 2.5 m). (a) Mean amplitude of the surface seasonal cycle; side panel: zonal mean ±1 standard deviation. (b) Month with the highest surface DIC. (c) Month with the lowest surface DIC. The latitude grid in (a) delimits the boundaries for the climate regions shown in Figure 6.

a location in the southern mid-latitudes (30.5°S, 60.5°E, marked in Figure 8b), that is, a location with an intermediate seasonality (Figure 8a). At this location, surface DIC increases from austral fall (March) to austral spring (September) and decreases again from austral spring to austral fall. The amplitude weakens with depth, and at about 75 m, the seasonal amplitude is nearly flat. Below that depth, which we refer to as the nodal depth, the phase of the seasonal cycle shifts, with the highest values occurring around austral fall (March) and the lowest values around austral spring (September). This pattern continues further down, but with progressively lower amplitude until the seasonal signal fades below 200 m.

The global distribution of the nodal depth of DIC reveals a distinct spatial pattern (Figure 8b). The nodal depth is relatively shallow across the entire tropics (shallower than ~50 m) and has a maximum near 30° latitude in both hemispheres with depths on the order of 250 m. The nodal depth at the higher latitudes varies greatly, with a mean depth on the order of 100 m. The deepest nodal depths are found in the northern North Atlantic, extending below 300 m.

Our estimate of the spatial distribution of the nodal depth is relatively patchy, and we find similar patchiness when computing the DIC nodal depth in our reconstruction with synthetic data (see supporting information Text S6). Nonetheless, the general pattern of the DIC nodal depth is well represented in our reconstruction with synthetic data.

The processes affecting the nodal depth are of both biological and physical nature. The nodal depth is linked to the vertical distribution of NCP. In the absence of any seasonality in mixing, the nodal depth occurs where NCP turns from positive to negative, that is, NCP = 0. Above this depth, primary production exceeds community respiration for most of the year, whereas below this depth, primary production is smaller than community respiration. The depth where this transition occurs is determined by how quickly primary production falls with depth and how rapidly community respiration increases by the remineralization of organic matter exported from shallower depths. This depth of zero NCP thus occurs where the depth profile of primary production crosses the depth profile of community respiration. This crossover usually happens at shallower depths than the depth of the euphotic zone (z_{eu}) (Sarmiento & Gruber, 2006), except in regions of very low productivity and export.

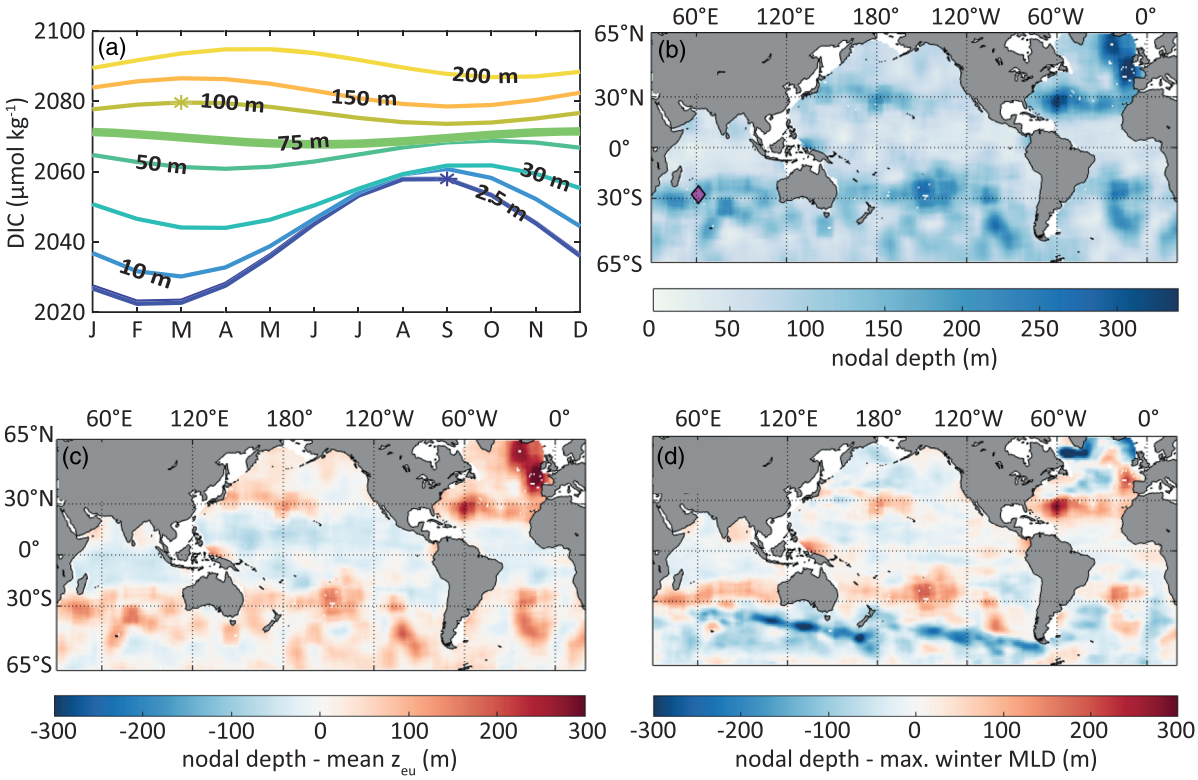

Figure 8. Analyses of the nodal depth of DIC. (a) The climatological seasonal cycle of DIC at various depths (indicated by color) at 30.5°S, 60.5°E (marked as a magenta diamond in b). The timings of the maximum DIC at the surface (September) and at 100 m (March) are marked with an asterisk, and the DIC at the nodal depth (75 m) is highlighted with a thick line. (b) Map of the nodal depth (m), smoothed with a filter that computes the mean of the neighboring ten grid cells. (c) Map of the difference between the nodal depth and annual mean depth of the euphotic zone (z_{eu}), determined from the 1% light level. (d) Map of the difference between the nodal depth and maximum winter MLD. Negative (blue) values indicate the nodal depth is shallower than z_{eu} or the winter MLD and positive (red) values indicate the nodal depth is deeper than z_{eu} or the winter MLD.

The nodal depth is also determined by the seasonal progression of the mixed layer. In many places, this mixing extends well below the depth of zero NCP, thereby modifying the nodal depth substantially. This displacement of the nodal depth depends sensitively on the seasonal timing of the mixed layer dynamics vis-á-vis the seasonal dynamics and depth distribution of NCP. On average, one expects the nodal depth to remain above the depth of the maximum winter MLD, except in regions where the depth of zero NCP is very deep.

These interactions between biological and physical drivers controlling the nodal depth become evident by inspecting the differences between the nodal depth and the depth of the euphotic zone (Figure 8c) and the nodal depth and the depth of maximum winter mixed layer (Figure 8d). Across most of the tropics, where the mixed layers tend to remain shallow throughout the seasons, we observe the nodal depth to be shallower than the depth of the euphotic zone. The distinct band of deep nodal depths at around 30° latitude is characterized by nodal depths that are deeper than either the euphotic zone or the winter MLD. We suspect that this is a consequence of relatively low production and export occurring at these latitudes, coupled with relatively deep winter mixed layers, pushing the nodal depth deep down. In the higher latitudes, the nodal depth tends to be primarily driven by the vertical mixing, with a complex pattern owing to the interaction between biology and mixing.

3.4. Spring-to-Fall NCP

The spring-to-fall NCP, inferred from the seasonal DIC drawdown between spring and fall (cf. Figure 5 while taking into account the contribution from air-sea gas exchange, vertical diffusion, and entrainment) is remarkably constant in the extra-tropical regions of the world's oceans (Figure 9). Between 23° to 65° in each hemisphere and between fall and spring, NCP is responsible for a mean carbon drawdown of ~1.9 ± 1.3 mol m^{-2} yr^{-1}. Summed up over this extra-tropical region, this mean rate corresponds to an integrated

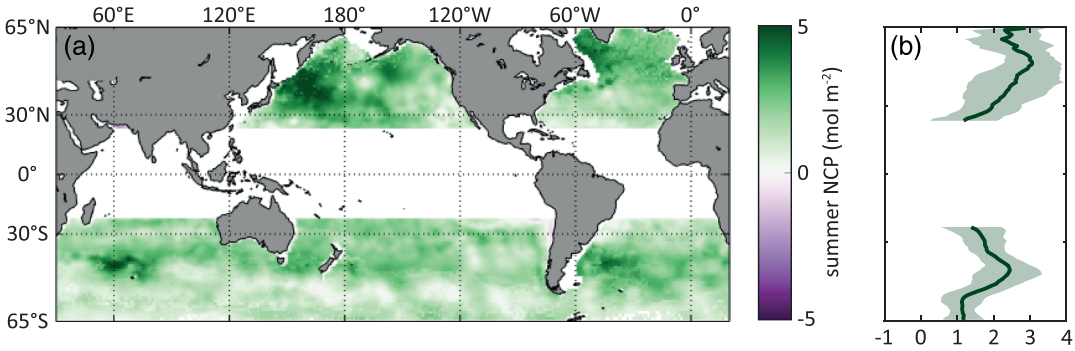

Figure 9. Analyses of the spring-to-fall NCP estimated from the seasonal drawdown of DIC. (a) Spatial distribution of depth-integrated spring-to-fall NCP between April and October (Northern Hemisphere) and between October and April (Southern Hemisphere). (b) Zonal mean spring-to-fall NCP, ±1 standard deviation. The region from 23°N to 23°S is masked due to the weak seasonal cycle here and the related high signal-to-noise ratio.

spring-to-fall NCP of 3.9 ± 2.7 Pg C yr^{-1} (Figure 9). The uncertainty ranges are based on the 68% obtained in Equation 6. We abstain from estimating NCP in the tropics because the seasonality there is small, resulting in a low signal-to-noise ratio that obscures our quantitative determination of NCP.

Assuming that the magnitude of the estimated NCP beyond the areas in which we calculate it is approximately the same as in the mid-latitudes, we upscale our estimate to the globe. Given the global ocean area of 361.9 · 10^6 km^2 (Eakins & Sharman, 2010), we arrive at a global spring-to-fall NCP of 8.2 ± 5.2 Pg C yr^{-1}. This is within the range of the findings by Lee (2001), who estimated the global spring-to-fall NCP to be 6.7 ± 2.7 or 8.0 ± 2.7 Pg C yr^{-1} over 8 months using two different methods. Our upscaled estimate only provides a rough estimate of the global spring-to-fall NCP and has added uncertainties compared to our spring-to-fall NCP estimate in the mid-latitudes.

We diagnose the largest spring-to-fall NCP in the Southern Ocean around 40°S, in the high-latitude North Atlantic (the Labrador Sea), and the northwestern Pacific (more than 5 ± 3.4 mol m^{-2} yr^{-1}). These three regions are areas of deep mixed layers and, thus, deep vertical mixing (Holte et al., 2017). The high values of spring-to-fall NCP in the northern North Atlantic are supported by the study by Körtzinger et al. (2008) who determined a spring-to-fall NCP of 6.4 ± 1.1 mol m^{-2} yr^{-1} for the high-latitude North Atlantic Ocean. Quay et al. (2012) found lower NCP in the subpolar North Atlantic, with an annual rate of 2.8 ± 2.7 mol m^{-2} yr^{-1}. However, the large uncertainty of this estimate precludes a more quantitative comparison.

Comparing our estimate of the spring-to-fall NCP to those from the long-running time series stations, we find a comparatively similar spring-to-fall NCP at the BATS site near Bermuda (Figure 1a). There, Gruber et al. (1998) estimated a spring-to-fall NCP of 1.4 mol m^{-2} yr^{-1} for the mixed layer, which corresponds to a spring-to-fall NCP of ~2.3 mol m^{-2} yr^{-1} for the entire euphotic zone, based on the assumption that 40% of the NCP occurs below the mixed layer (Gruber et al., 1998). Our MOBO-DIC-based estimate of 1.5 ± 1.0 mol m^{-2} yr^{-1} at BATS is thus on the low side, although not significantly different. One potential reason for the difference is that Gruber et al. (1998) took lateral advection into account and found this to be a source of DIC at the BATS site. Thus, neglecting the lateral advection in our estimate results in an underestimation of the DIC there. Similarly, Keeling et al. (2004) and Quay and Stutsman (2003) estimated the NCP at the HOT site near Hawaii (Figure 1a) using a diagnostic mixed layer model. This site is at 22°N, and so it is technically excluded in our NCP estimate. Nonetheless, we compare it here as it is very close to the boundary of our cutoff at 23°N. Keeling et al. (2004) and Quay and Stutsman (2003) estimate the annual NCP in the mixed layer at the HOT site as 2.3 ± 0.8 and 2.6 ± 1.3 mol m^{-2} yr^{-1}, respectively. Keeling et al. (2004) extrapolated their estimate over the euphotic zone, where they obtain an NCP of 2.8 mol m^{-2} yr^{-1}. Our estimate at that location is 2.0 ± 1.4 mol m^{-2} yr^{-1} over the summer, which is close to that estimate, especially when considering the additional NCP over the winter. Ocean Station Papa in the northeastern Pacific (OSP; 50°N, 145°W) comprises another station where NCP was historically estimated, although in contrast to our study, from nitrate and oxygen.

Plant et al. (2016) estimate an annual NCP at station OSP of 1.5 ± 0.7 mol m^{-2} yr^{-1}, which is within the range of our estimated spring-to-fall NCP of 2.5 ± 1.7 mol m^{-2} yr^{-1}. However, their estimate includes the full year, and we speculate that it would be lower than our estimate when only considering the summer months. One

long-running station where NCP is estimated in the Southern Ocean is the Drake Passage, that is, between the South American Coast and the Antarctic Continent (see Figure 1a). Munro, Lovenduski, Stephens, et al. (2015) estimate the NCP in the Drake Passage using seasonal measurements of phosphate and DIC resulting in an annual NCP of 1.2 ± 0.7 and $1.6 \pm 0.4\,\mathrm{mol\,m^{-2}\,yr^{-1}}$, depending on the method used. We derive a spring-to-fall NCP estimate in the Drake Passage of $1.5 \pm 1.0\,\mathrm{mol\,m^{-2}\,yr^{-1}}$, which is reasonably close to the findings by Munro, Lovenduski, Stephens, et al. (2015), with the difference linked to the fact that we only include the DIC drawdown in the summer months. NCP in the Southern Ocean has been further reported Brix et al. (2013) at the Munida time series east of New Zealand's South Island. These authors report an annual NCP of $1.2 \pm 0.7\,\mathrm{mol\,m^{-2}\,yr^{-1}}$, which is equally close to our estimate of $1.3 \pm 0.9\,\mathrm{mol\,m^{-2}\,yr^{-1}}$ taken from our estimate at the grid point closest to the Munida time series station.

The degree to which NCP varies across the open ocean has been the subject of a substantial scientific debate. Emerson and Bushinsky (2014) were among the first to marvel about the fact that despite large differences in chlorophyll and net primary productivity (NPP); NCP varies little between the subtropical sites HOT and BATS and the subpolar North Pacific site OSP. Ostle et al. (2015) also found a relatively constant NCP across the Atlantic north of 35°N. When tabulating the NCP estimates from the other sites discussed in the previous paragraph, the Drake Passage and Munida sites in the Southern Hemisphere, the relatively small spread of NCP stands out: NCP varies only between about 1 and $3\,\mathrm{mol\,m^{-2}\,yr^{-1}}$ across these sites. Our approach now permits us to add new information to this debate, as it provides a large-scale perspective to the local studies.

To the first order, our diagnosed values also confirm a relatively uniform distribution of NCP, especially when comparing to the spatial variations in chlorophyll. NCP varies spatially by about a factor of 5, while chlorophyll varies by a factor of 100 or more. Compared to net primary production, which varies by a factor of 10 (Behrenfeld & Falkowski, 1997), NCP varies less. Still, we find distinct variations in our diagnosed NCP, even in the zonal mean. Figure 9b reveals a tendency for an increase in NCP with latitude in the Northern Hemisphere. This is inconsistent with the results of Ostle et al. (2015) but is supported by the results from Körtzinger et al. (2008) and Quay et al. (2012) for the subpolar North Atlantic. Additionally, the Southern Hemisphere has a distinct trend in the zonal mean, with increasing values poleward of the tropics and a maximum around 45°S. This is followed by a strong decrease in the high latitudes of the Southern Ocean. The uncertainties in our estimates are substantial, but the good agreement with the local estimates from numerous time series sites provides some confirmation that the estimates are reasonable. The spatial distribution of our diagnosed NCP is very similar to that found by Lee (2001), who also used the seasonal DIC drawdown as a constraint for NCP. They also found a distinct maximum of NCP in the mid-latitude Southern Hemisphere, although slightly further south than our estimate. One reason for this difference is that they inferred NCP from surface DIC data only, whereas we estimate NCP across the euphotic zone.

In summary, our seasonal DIC climatology extending throughout the upper ocean allows us to extend the geochemical constraint on NCP emerging from the spring to fall drawdown of DIC to the global scale. So far, its application was limited to the local level, owing to the requirement of having well-established time series observations of DIC. Our fully mapped product permits us to diagnose NCP throughout the global extra-tropical ocean. However, our estimate here is only a first step. This approach can be refined by improving the estimates for the contribution from the other processes, namely, air-sea gas exchange, vertical diffusion, and entrainment. Especially important is to account for the potential contribution by lateral transport and mixing, which has been demonstrated to be relevant at numerous locations (Gruber et al., 1998; Keeling et al., 2004).

4. Summary

We created a global monthly climatology of MOBO-DIC based on measurements from the repeat hydrography synthesis project GLODAPv2.2019 (Olsen et al., 2019). Using a two-step neural network mapping technique, we first clustered the global ocean into regions of similar biogeochemical properties and statistical relationships with SOMs and then ran an FFN in each cluster using various physical and biogeochemical parameters as predictor data. The resulting monthly climatology is mapped on a $1° \times 1°$ grid from 65°N to 65°S on 33 depth levels from 2.5 to 1,975 m and is based on data from 2004 through 2017.

We test our results in various ways, including with synthetic data from the biogeochemical component of the Ocean General Circulation Model HAMOCC, an existing DIC climatology (Lauvset et al., 2016),

independent time series station data (HOT, BATS, and Drake Passage), as well as measurements from SOCCOM floats. We find that our method performs well in estimating the mean monthly DIC fields, demonstrated by the RMSEs between our estimate and the independent validation data being below 30 μmol kg^{-1}. A large part of the discrepancies near the surface stems from differences in the time period of the validation data and our estimate of DIC. At the location of the independent observational data, our estimate of DIC is always considerably closer to the independent measurements than the DIC in HAMOCC, suggesting that our method provides a better estimate for the observed seasonal cycle than the model.

We estimate a global DIC inventory of ~37,000 Pg C (37,214 ± 195 Pg C), which is significantly lower than previous estimates based on sparse observations. In our MOBO-DIC climatology, the global mean DIC concentration increases from ~2,044 ± 69 μmol kg^{-1} at the surface to ~2,270 ± 68 μmol kg^{-1} at 1,975 m. While the top ~500 m exhibits distinct spatial features because of the large-scale circulation interacting with the biological pumps, the deeper waters have a more uniform DIC concentration.

The seasonal cycle of DIC has the largest amplitudes at the high northern latitudes (~30 to more than 50 μmol kg^{-1}). The remaining global ocean, including the high southern latitudes, has a median amplitude of ~14 μmol kg^{-1}. In both hemispheres, the months of the highest DIC tend to be in hemispheric spring, when vertical mixing is usually deepest, while the lowest DIC concentrations tend to be in hemispheric fall, linked to the biological drawdown of DIC between hemispheric spring and fall.

The nodal depth of DIC, where the phase of the seasonal cycle of DIC shifts by 6 months, is deepest in the North Atlantic and at around 30° latitude (more than 250 m), while it is relatively shallow in the tropics (less than 100 m). This distribution is linked to the vertical distribution of NCP but is strongly modified by the seasonal cycle of the MLD. In regions of low mixing, the nodal depth is determined by the depth where NCP changes sign from positive to negative. This depth is typically located within the euphotic zone, as seen in the tropics. Exceptions are regions of very low productivity, where the nodal depth could be much deeper, explaining in part the deep nodal depths at 30° latitudes. The deep and very variable nodal depths of the extra-tropics are likely a result of the complex interaction of the winter mixing with the seasonal cycle of NCP.

From the spring-to-fall DIC drawdown, we diagnose a relatively homogeneous distribution of extra-tropical spring-to-fall NCP with a mean value of 1.9 ± 1.3 mol m^{-2} yr^{-1}, very consistent with a large range of estimates from numerous time series study sites. The largest spring-to-fall NCP occurs in areas of deep vertical mixing (e.g., around 40°S, and in the northern high-latitude Atlantic and West Pacific), in line with previous estimates based on in situ data. Our estimate suggests a weak but significant increase in spring-to-fall NCP with increasing latitude in the Northern Hemisphere. Conversely, in the Southern Hemisphere, the maximum spring-to-fall NCP can be found around 40°S with the lowest NCP in the high latitudes of the Southern Ocean.

MOBO-DIC provides an advancement to previous DIC climatologies that were either limited by the lack of seasonality (Lauvset et al., 2016) or by the lack of the depth domain (Gregor & Gruber, 2020; Lee, 2001; Sasse et al., 2013). It provides a baseline to initialize model setups, study the seasonal cycle of DIC and its future changes linked to ocean acidification, and determine the physical and biogeochemical drivers of the marine carbon cycle. Our DIC-derived spring-to-fall NCP estimate in the mid-latitudes of 1.9 ± 1.3 mol m^{-2} yr^{-1} (~3.9 ± 2.7 Pg C yr^{-1}), and our upscaled global estimate of 8.2 ± 5.6 Pg C yr^{-1} is in line with previous observation-based assessments and serves as a complementary approach to estimates based on oxygen (e.g., Emerson & Bushinsky, 2014; Emerson et al., 2008; Ostle et al., 2015), remote sensing (Li & Cassar, 2016), inverse models (DeVries & Weber, 2017; Schlitzer, 2004), and other approaches.

Data Availability Statement

The data product created during this study is freely available from NCEI/OCADS: https://www.ncei.noaa.gov/access/ocean-carbon-data-system/oceans/ndp_104/ndp104.html and should be cited as Keppler et al. (2020). Mapped Observation-Based Oceanic dissolved inorganic carbon (DIC), monthly climatology, from January to December (based on observations between 2004 and 2017), from the Max-Planck-Institute for Meteorology (MOBO-DIC_MPIM) (NCEI Accession 0221526) (indicate subset used). NOAA National Centers for Environmental Information Dataset (https://doi.org/10.25921/yvzj-zx46) accessed (date).

Acknowledgments
The research leading to these results has received funding from the European Community's Horizon 2020 Project under grant agreement no. 821003 (4C). L. K. gratefully acknowledges funding from the International Max Planck Research School on Earth System Modelling (IMPRS-ESM). The authors are grateful for the Argo data collected and made freely available by the International Argo Program and the national programs that contribute to it (https://www.argo.ucsd.edu and https://argo.jcommops.org). The Argo Program is part of the Global Ocean Observing System. This publication uses Hawaii Ocean Time-series observations supported by the U.S. National Science Foundation under Grant OCE-1260164. It also used data from the Southern Ocean Carbon and Climate Observations and Modeling project (SOCCOM). Data were collected and made freely available by SOCCOM funded by the National Science Foundation, Division of Polar Programs (NSF PLR-1425989), supplemented by NASA and by the International Argo Program and the NOAA programs that contribute to it. This work benefited from discussions with Birgit Klein (BSH), Jochem Marotzke (MPI-M), Johanna Baehr (UHH), Jens Müller (IOW), and Katharina Six (MPI-M). Open access funding enabled and organized by Projekt DEAL.

References

Amante, C., & Eakins, B. W. (2009). ETOPO1 1 arc-minute global relief model: Procedures, data sources and analysis. NOAA Technical Memorandum NESDIS NGDC-24. National Geophysical Data Center.

Argo (2019). Argo float data and metadata from Global Data Assembly Centre (Argo GDAC). SEANOE, type: Dataset.

Bates, N. R. (2001). Interannual variability of oceanic CO_2 and biogeochemical properties in the Western North Atlantic subtropical gyre. *Deep Sea Research Part II: Topical Studies in Oceanography*, *48*(8), 1507–1528. https://doi.org/10.1016/S0967-0645(00)00151-X

Bates, N. R., Astor, Y. M., Church, M. J., Currie, K., Dore, J. E., Gonzalez-Davila, M., et al. (2014). A time-series view of changing surface ocean chemistry due to ocean uptake of anthropogenic CO_2 and ocean acidification. *Oceanography*, *27*(1), 126–141. https://doi.org/10.5670/oceanog.2014.16

Bates, N. R., Michaels, A. F., & Knap, A. H. (1996). Seasonal and interannual variability of oceanic carbon dioxide species at the U.S. JGOFS Bermuda Atlantic Time-series Study (BATS) site. *Deep Sea Research Part II: Topical Studies in Oceanography*, *43*(2), 347–383. https://doi.org/10.1016/0967-0645(95)00093-3

Behrenfeld, M. J., & Falkowski, P. G. (1997). A consumer's guide to phytoplankton primary productivity models. *Limnology and Oceanography*, *42*(7), 1479–1491. https://doi.org/10.4319/lo.1997.42.7.1479

Bittig, H. C., Steinhoff, T., Claustre, H., Fiedler, B., Williams, N. L., Sauzède, R., et al. (2018). An alternative to static climatologies: Robust estimation of open ocean CO_2 variables and nutrient concentrations from T, S, and O_2 data using Bayesian Neural Networks. *Frontiers in Marine Science*, *5*, 328. https://doi.org/10.3389/fmars.2018.00328

Boyd, P. (2019). Multi-faceted particle pumps drive carbon sequestration in the ocean. *Nature*, *568*(7752), 327–335. https://doi.org/10.1038/s41586-019-1098-2

Brewer, P. G. (1978). Direct observation of the oceanic CO_2 increase. *Geophysical Research Letters*, *5*(12), 997–1000. https://doi.org/10.1029/GL005i012p00997

Brix, H., Currie, K. I., & Mikaloff Fletcher, S. E. (2013). Seasonal variability of the carbon cycle in subantarctic surface water in the South West Pacific. *Global Biogeochemical Cycles*, *27*, 200–211. https://doi.org/10.1002/gbc.20023

Brix, H., Gruber, N., & Keeling, C. D. (2004). Interannual variability of the upper ocean carbon cycle at station ALOHA near Hawaii. *Global Biogeochemical Cycles*, *18*, GB4019. https://doi.org/10.1029/2004GB002245

Broullón, D., Pérez, F. F., Velo, A., Hoppema, M., Olsen, A., Takahashi, T., et al. (2019). A global monthly climatology of total alkalinity: A neural network approach. *Earth System Science Data*, *11*(3), 1109–1127. https://doi.org/10.5194/essd-11-1109-2019

Broullón, D., Pérez, F. F., Velo, A., Hoppema, M., Olsen, A., Takahashi, T., et al. (2020). A global monthly climatology of oceanic total dissolved inorganic carbon: A neural network approach. *Earth System Science Data*, *12*(3), 1725–1743. https://doi.org/10.5194/essd-12-1725-2020

Bushinsky, S. M., Landschützer, P., Rödenbeck, C., Gray, A. R., Baker, D., Mazloff, M. R., et al. (2019). Reassessing Southern Ocean air-sea CO_2 flux estimates with the addition of biogeochemical float observations. *Global Biogeochemical Cycles*, *33*, 1370–1388. https://doi.org/10.1029/2019GB006176

Carter, B. R., Feely, R. A., Williams, N. L., Dickson, A. G., Fong, M. B., & Takeshita, Y. (2018). Updated methods for global locally interpolated estimation of alkalinity, pH, and nitrate. *Limnology and Oceanography: Methods*, *16*(2), 119–131. https://doi.org/10.1002/lom3.10232

Chen, G.-T., & Millero, F. J. (1979). Gradual increase of oceanic CO_2. *Nature*, *277*(5693), 205–206. https://doi.org/10.1038/277205a0

Ciais, P., Sabine, C., Bala, G., Bopp, L., Brovkin, V., Canadell, J., et al. (2014). Carbon and other biogeochemical cycles, *Climate change 2013: The physical science basis. Contribution of Working Group I to the Fifth Assessment Report of the Intergovernmental Panel on Climate Change* (pp. 465–570). Cambridge: Cambridge University Press.

DeVries, T., & Weber, T. (2017). The export and fate of organic matter in the ocean: New constraints from combining satellite and oceanographic tracer observations. *Global Biogeochemical Cycles*, *31*, 535–555. https://doi.org/10.1002/2016GB005551

Denman, K. L., & Gargett, A. E. (1983). Time and space scales of vertical mixing and advection of phytoplankton in the upper ocean. *Limnology and Oceanography*, *28*(5), 801–815. https://doi.org/10.4319/lo.1983.28.5.0801

Dibike, Y. B., & Coulibaly, P. (2006). Temporal neural networks for downscaling climate variability and extremes. *Neural Networks*, *19*(2), 135–144. https://doi.org/10.1016/j.neunet.2006.01.003

Dillon, T. M., & Caldwell, D. R. (1980). The batchelor spectrum and dissipation in the upper ocean. *Journal of Geophysical Research*, *85*, 1910–1916. https://doi.org/10.1029/JC085iC04p01910

Dore, J. E., Lukas, R., Sadler, D. W., Church, M. J., & Karl, D. M. (2009). Physical and biogeochemical modulation of ocean acidification in the central north pacific. *Proceedings of the National Academy of Sciences of the United States of America*, *106*(30), 12,235–12,240. https://doi.org/10.1073/pnas.0906044106

Dore, J. E., Lukas, R., Sadler, D. W., & Karl, D. M. (2003). Climate-driven changes to the atmospheric CO_2 sink in the subtropical North Pacific ocean. *Nature*, *424*(6950), 754–757. https://doi.org/10.1038/nature01885

Eakins, B. W., & Sharman, G. F. (2010). Volumes of the world's oceans from ETOPO1. https://www.ngdc.noaa.gov/mgg/global/etopo1_ocean_volumes.html, NOAA National Geophysical Data Center, Boulder, CO.

Emerson, S. (2014). Annual net community production and the biological carbon flux in the ocean. *Global Biogeochemical Cycles*, *28*, 14–28. https://doi.org/10.1002/2013GB004680

Emerson, S., & Bushinsky, S. (2014). Oxygen concentrations and biological fluxes in the open ocean. *Oceanography*, *27*(1), 168–171. https://doi.org/10.5670/oceanog.2014.20

Emerson, S., Stump, C., & Nicholson, D. (2008). Net biological oxygen production in the ocean: Remote in situ measurements of O_2 and N_2 in surface waters. *Global Biogeochemical Cycles*, *22*, GB3023. https://doi.org/10.1029/2007GB003095

Feely, R. A., Takahashi, T., Wanninkhof, R., McPhaden, M. J., Cosca, C. E., Sutherland, S. C., & Carr, M.-E. (2006). Decadal variability of the air-sea CO_2 fluxes in the equatorial pacific ocean. *Journal of Geophysical Research*, *111*, C08S90. https://doi.org/10.1029/2005JC003129

Friedlingstein, P., Jones, M. W., O'Sullivan, M., Andrew, R. M., Hauck, J., Peters, G. P., et al. (2019). Global carbon budget 2019. *Earth System Science Data*, *11*(4), 1783–1838. https://doi.org/10.5194/essd-11-1783-2019

Garcia, H. E., Boyer, T. P., Baranova, O. K., Locarnini, R. A., Mishonov, A. V., Paver, C. R., et al. (2019). World ocean atlas 2018: Product documentation.

Gardner, M. W., & Dorling, S. R. (1998). Artificial neural networks (the multilayer perceptron)—A review of applications in the atmospheric sciences. *Atmospheric Environment*, *32*, 2627–2636. https://doi.org/10.1016/S1352-2310(97)00447-0

Gervais, F., Riebesell, U., & Gorbunov, M. Y. (2002). Changes in primary productivity and chlorophyll a in response to iron fertilization in the southern polar frontal zone. *Limnology and Oceanography*, *47*(5), 1324–1335. https://doi.org/10.4319/lo.2002.47.5.1324

Gray, A. R., Johnson, K. S., Bushinsky, S. M., Riser, S. C., Russell, J. L., Talley, L. D., et al. (2018). Autonomous biogeochemical floats detect significant carbon dioxide outgassing in the high-latitude Southern Ocean. *Geophysical Research Letters*, *45*, 9049–9057. https://doi.org/10.1029/2018GL078013

Gregor, L., & Gruber, N. (2020). OceanSODA-ETHZ: A global gridded data set of the surface ocean carbonate system for seasonal to decadal studies of ocean acidification. *Earth System Science Data Discussions*, 1–42. https://doi.org/10.5194/essd-2020-300

Gruber, N., Clement, D., Carter, B. R., Feely, R. A., Heuven, S., Hoppema, M., et al. (2019). The oceanic sink for anthropogenic CO_2 from 1994 to 2007. *Science*, *363*(6432), 1193–1199. https://doi.org/10.1126/science.aau5153

Gruber, N., Keeling, C. D., & Bates, N. R. (2002). Interannual variability in the North Atlantic Ocean carbon sink. *Science*, *298*(5602), 2374. https://doi.org/10.1126/science.1077077

Gruber, N., Keeling, C. D., & Stocker, T. F. (1998). Carbon-13 constraints on the seasonal inorganic carbon budget at the BATS site in the northwestern Sargasso Sea. *Deep Sea Research Part I: Oceanographic Research Papers*, *45*(4), 673–717. https://doi.org/10.1016/S0967-0637(97)00098-8

Gruber, N., & Sarmiento, J. L. (2002). Large-scale biogeochemical-physical interactions in elemental cycles. In A. R. Robinson, J. J. McCarthy, B. J. Rothschild (Eds.), *The Sea: Ideas and observations on progress in the study of the seas* (Vol. 12). Cambridge: Harvard University Press.

Gruber, N., Sarmiento, J. L., & Stocker, T. F. (1996). An improved method for detecting anthropogenic CO_2 in the oceans. *Global Biogeochemical Cycles*, *10*(4), 809–837. https://doi.org/10.1029/96GB01608

Hagan, M. T., Demuth, H. B., Beale, M. H., & De Jess, O. (2014). *Neural network design* (2nd ed.). Stillwater, Oklahoma: Martin Hagan.

Hauck, J., & Voelker, C. (2015). Rising atmospheric CO_2 leads to large impact of biology on Southern Ocean CO_2 uptake via changes of the Revelle factor. *Geophysical Research Letters*, *42*, 1459–1464. https://doi.org/10.1002/2015GL063070

Heinze, C., Meyer, S., Goris, N., Anderson, L., Steinfeldt, R., Chang, N., et al. (2015). The ocean carbon sink impacts, vulnerabilities and challenges. *Earth System Dynamics*, *6*(1), 327–358. https://doi.org/10.5194/esd-6-327-2015

Holte, J., Talley, L. D., Gilson, J., & Roemmich, D. (2017). An Argo mixed layer climatology and database. *Geophysical Research Letters*, *44*, 5618–5626. https://doi.org/10.1002/2017GL073426

Hornik, K., Stinchcombe, M., & White, H. (1989). Multilayer feedforward networks are universal approximators. *Neural Networks*, *2*(5), 359–366. https://doi.org/10.1016/0893-6080(89)90020-8

Ilyina, T., Six, K. D., Segschneider, J., Maier Reimer, E., Li, H., & Nez Riboni, I. (2013). Global ocean biogeochemistry model HAMOCC: Model architecture and performance as component of the MPI-Earth system model in different CMIP5 experimental realizations. *Journal of Advances in Modeling Earth Systems*, *5*, 287–315. https://doi.org/10.1029/2012MS000178

Jenkins, W. J., & Goldman, J. C. (1985). Seasonal oxygen cycling and primary production in the Sargasso Sea. *Journal of Marine Research*, *43*, 465–491.

Juranek, L. W., Quay, P. D., Feely, R. A., Lockwood, D., Karl, D. M., & Church, M. J. (2012). Biological production in the NE Pacific and its influence on air-sea CO_2 flux: Evidence from dissolved oxygen isotopes and O_2 /ar. *Journal of Geophysical Research*, *117*, C05022. https://doi.org/10.1029/2011JC007450

Keeling, C. D. (1993). NATO lecture 2: Surface ocean CO_2, *The global carbon cycle* (pp. 413–429). Berlin, Heidelberg: Springer.

Keeling, C. D., Brix, H., & Gruber, N. (2004). Seasonal and long-term dynamics of the upper ocean carbon cycle at station ALOHA near Hawaii. *Global Biogeochemical Cycles*, *18*, GB4006. https://doi.org/10.1029/2004GB002227

Keppler, L., & Landschützer, P. (2019). Regional wind variability modulates the Southern Ocean carbon sink. *Scientific Reports*, *9*(1), 1–10. https://doi.org/10.1038/s41598-019-43826-yv

Keppler, L., Landschützer, P., Gruber, N., Lauvset, S. K., & Stemmler, I. (2020). Mapped Observation-Based Oceanic dissolved inorganic carbon (DIC), monthly climatology, from January to December (based on observations between 2004 and 2017), from the Max-Planck-Institute for Meteorology (MOBO-DIC_MPIM) (NCEI Accession 0221526). NOAA National Centers for Environmental Information. Dataset, https://www.ncei.noaa.gov/access/ocean-carbon-data-system/oceans/ndp_104/ndp104.html

Kohonen, T. (1989). *Self-organization and associative memory* (3rd ed.). Berlin, Heidelberg: Springer.

Kohonen, T. (2001). *Self-organizing maps, Springer Series in Information Sciences*. Berlin, Heidelberg: Springer.

Körtzinger, A., Send, U., Lampitt, R. S., Hartman, S., Wallace, D. W. R., Karstensen, J., et al. (2008). The seasonal pCO_2 cycle at 49°N/16.5°W in the northeastern Atlantic Ocean and what it tells us about biological productivity. *Journal of Geophysical Research*, *113*, C04020. https://doi.org/10.1029/2007JC004347

Kwiatkowski, L., Aumont, O., Bopp, L., & Ciais, P. (2018). The impact of variable phytoplankton stoichiometry on projections of primary production, food quality, and carbon uptake in the global ocean. *Global Biogeochemical Cycles*, *32*, 516–528. https://doi.org/10.1002/2017GB005799

Landschützer, P., Gruber, N., Bakker, D. C. E., & Schuster, U. (2014). Recent variability of the global ocean carbon sink. *Global Biogeochemical Cycles*, *28*, 927–949. https://doi.org/10.1002/2014GB004853

Landschützer, P., Gruber, N., Bakker, D. C. E., Schuster, U., Nakaoka, S., Payne, M. R., et al. (2013). A neural network-based estimate of the seasonal to inter-annual variability of the Atlantic Ocean carbon sink. *Biogeosciences*, *10*(11), 7793–7815. https://doi.org/10.5194/bg-10-7793-2013

Landschützer, P., Gruber, N., Bakker, D. C. E., Stemmler, I., & Six, K. D. (2018). Strengthening seasonal marine CO_2 variations due to increasing atmospheric CO_2. *Nature Climate Change*, *8*(2), 146–150. https://doi.org/10.1038/s41558-017-0057-x

Lauvset, S. K., Key, R. M., Olsen, A., van Heuven, S., Velo, A., Lin, X., et al. (2016). A new global interior ocean mapped climatology: The 1° × 1° GLODAP version 2. *Earth System Science Data*, *8*(2), 325–340. https://doi.org/10.5194/essd-8-325-2016

Le Quéré, C., Andrew, R. M., Friedlingstein, P., Sitch, S., Pongratz, J., Manning, A. C., et al. (2018). Global carbon budget 2017. *Earth System Science Data*, *10*(1), 405–448. https://doi.org/10.5194/essd-10-405-2018

Lee, K. (2001). Global net community production estimated from the annual cycle of surface water total dissolved inorganic carbon. *Limnology and Oceanography*, *46*(6), 1287–1297. https://doi.org/10.4319/lo.2001.46.6.1287

Li, Z., & Cassar, N. (2016). Satellite estimates of net community production based on O_2/ar observations and comparison to other estimates. *Global Biogeochemical Cycles*, *30*, 735–752. https://doi.org/10.1002/2015GB005314

Lozovatsky, I. D., Fernando, H. J. S., & Shapovalov, S. M. (2008). Deep-ocean mixing on the basin scale: Inference from North Atlantic transects. *Deep Sea Research Part I: Oceanographic Research Papers*, *55*(9), 1075–1089. https://doi.org/10.1016/j.dsr.2008.05.003

Mauritsen, T., Bader, J., Becker, T., Behrens, J., Bittner, M., Brokopf, R., et al. (2019). Developments in the MPI-M Earth System Model version 1.2 (MPI-ESM1.2) and its response to increasing CO_2. *Journal of Advances in Modeling Earth Systems*, *11*, 998–1038. https://doi.org/10.1029/2018MS001400

McNeil, B. I., & Sasse, T. P. (2016). Future ocean hypercapnia driven by anthropogenic amplification of the natural CO_2 cycle. *Nature*, *529*(7586), 383–386. https://doi.org/10.1038/nature16156

Michaels, A. F., Bates, N. R., Buesseler, K. O., Carlson, C. A., & Knap, A. H. (1994). Carbon-cycle imbalances in the Sargasso Sea. *Nature*, *372*(6506), 537–540. https://doi.org/10.1038/372537a0

Mongwe, N. P., Vichi, M., & Monteiro, P. M. S. (2018). The seasonal cycle of pCO_2 and CO_2 fluxes in the Southern Ocean: Diagnosing anomalies in CMIP5 Earth System Models. *Biogeosciences*, *15*(9), 2851–2872. https://doi.org/10.5194/bg-15-2851-2018

Morel, A., Huot, Y., Gentili, B., Werdell, P. J., Hooker, S. B., & Franz, B. A. (2007). Examining the consistency of products derived from various ocean color sensors in open ocean (Case 1) waters in the perspective of a multi-sensor approach. *Remote Sensing of Environment*, *111*, 69–88. https://doi.org/10.1016/j.rse.2007.03.012

Munro, D. R., Lovenduski, N. S., Stephens, B. B., Newberger, T., Arrigo, K. R., Takahashi, T., et al. (2015). Estimates of net community production in the Southern Ocean determined from time series observations (2002–2011) of nutrients, dissolved inorganic carbon, and surface ocean pCO_2 in Drake Passage. *Deep Sea Research Part II: Topical Studies in Oceanography*, *114*, 49–63. https://doi.org/10.1016/j.dsr2.2014.12.014

Munro, D. R., Lovenduski, N. S., Takahashi, T., Stephens, B. B., Newberger, T., & Sweeney, C. (2015). Recent evidence for a strengthening CO_2 sink in the Southern Ocean from carbonate system measurements in the Drake Passage (2002–2015). *Geophysical Research Letters*, *42*, 7623–7630. https://doi.org/10.1002/2015GL065194

Najjar, R. G., & Keeling, R. F. (1997). Analysis of the mean annual cycle of the dissolved oxygen anomaly in the world ocean. *Journal of Marine Research*, *55*, 117–151. https://doi.org/10.1357/0022240973224481

Nevison, C. D., Manizza, M., Keeling, R. F., Stephens, B. B., Bent, J. D., Dunne, J., et al. (2016). Evaluating CMIP5 ocean biogeochemistry and Southern Ocean carbon uptake using atmospheric potential oxygen: Present-day performance and future projection. *Geophysical Research Letters*, *43*, 2077–2085. https://doi.org/10.1002/2015GL067584

Olsen, A., Lange, N., Key, R. M., Tanhua, T., Álvarez, M., Becker, S., et al. (2019). GLODAPv2.2019 – an update of GLODAPv2. *Earth System Science Data*, *11*(3), 1437–1461. https://doi.org/10.5194/essd-11-1437-2019

Ostle, C., Johnson, M., Landschützer, P., Schuster, U., Hartman, S., Hull, T., & Robinson, C. (2015). Net community production in the North Atlantic Ocean derived from volunteer observing ship data. *Global Biogeochemical Cycles*, *29*, 80–95. https://doi.org/10.1002/2014GB004868

Paulmier, A., Ruiz-Pino, D., & Garçon, V. (2011). CO_2 maximum in the oxygen minimum zone (OMZ). *Biogeosciences*, *8*(2), 239–252. https://doi.org/10.5194/bg-8-239-2011

Plant, J. N., Johnson, K. S., Sakamoto, C. M., Jannasch, H. W., Coletti, L. J., Riser, S. C., & Swift, D. D. (2016). Net community production at ocean station papa observed with nitrate and oxygen sensors on profiling floats. *Global Biogeochemical Cycles*, *30*, 859–879. https://doi.org/10.1002/2015GB005349

Prentice, I. C., Farquhar, G. D., Fasham, M. J. R., Goulden, M. L., Heimann, M., Jaramillo, V. J., et al. (2001). The carbon cycle and atmospheric carbon dioxide. Climate Change 2001: The Scientific Basis, 183–237.

Quay, P., & Stutsman, J. (2003). Surface layer carbon budget for the subtropical N. Pacific: $\delta^{13}C$ constraints at station ALOHA. *Deep Sea Research Part I: Oceanographic Research Papers*, *50*(9), 1045–1061. https://doi.org/10.1029/2010GB004003

Quay, P., Stutsman, J., & Steinhoff, T. (2012). Primary production and carbon export rates across the subpolar N. Atlantic Ocean basin based on triple oxygen isotope and dissolved O_2 and Ar gas measurements. *Global Biogeochemical Cycles*, *26*, GB2003. https://doi.org/10.1029/2010GB004003

Riser, S. C., & Johnson, K. S. (2008). Net production of oxygen in the subtropical ocean. *Nature*, *451*(7176), 323–325. https://doi.org/10.1038/nature06441

Rödenbeck, C., Bakker, D. C. E., Gruber, N., Iida, Y., Jacobson, A. R., Jones, S., et al. (2015). Data-based estimates of the ocean carbon sink variability âĂŞ first results of the surface ocean pCO_2 mapping intercomparison (SOCOM). *Biogeosciences*, *12*(23), 7251–7278. https://doi.org/10.5194/bg-12-7251-2015

Rodgers, K. B., Aumont, O., Menkes, C., & Gorgues, T. (2008). Decadal variations in equatorial Pacific ecosystems and ferrocline/pycnocline decoupling. *Global Biogeochemical Cycles*, *22*, GB2019. https://doi.org/10.1029/2006GB002919

Roemmich, D., & Gilson, J. (2009). The 2004-2008 mean and annual cycle of temperature, salinity, and steric height in the global ocean from the Argo program. *Progress in Oceanography*, *82*(2), 81–100. https://doi.org/10.1016/j.pocean.2009.03.004

Roobaert, A., Laruelle, G. G., Landschützer, P., Gruber, N., Chou, L., & Regnier, P. (2019). The spatiotemporal dynamics of the sources and sinks of CO_2 in the global coastal ocean. *Global Biogeochemical Cycles*, *33*, 1693–1714. https://doi.org/10.1029/2019GB006239

Sabine, C. L., Feely, R. A., Gruber, N., Key, R. M., Lee, K., Bullister, J. L., et al. (2004). The oceanic sink for anthropogenic CO_2. *Science*, *305*(5682), 367–371. https://doi.org/10.1126/science.1097403

Sabine, C. L., & Tanhua, T. (2010). Estimation of anthropogenic CO_2 inventories in the ocean. *Annual Review of Marine Science*, *2*, 175–198. https://doi.org/10.1146/annurev-marine-120308-080947

Sarma, V. V. S. S., Lenton, A., Law, R. M., Metzl, N., Patra, P. K., Doney, S., et al. (2013). Sea-air CO_2 fluxes in the Indian Ocean between 1990 and 2009. *Biogeosciences*, *10*(11), 7035–7052. https://doi.org/10.5194/bg-10-7035-2013

Sarmiento, J. L., & Gruber, N. (2002). Sinks for anthropogenic carbon. *Physics Today*, *55*(8), 30–36. https://doi.org/10.1063/1.1510279

Sarmiento, J. L., & Gruber, N. (2006). Carbon cycle, CO_2, and climate; The anthropogenic perturbation, *Ocean biogeochemical dynamics* (pp. 399–417). Princeton: Princeton University Press.

Sasse, T. P., McNeil, B. I., & Abramowitz, G. (2013). A new constraint on global air-sea CO_2 fluxes using bottle carbon data. *Geophysical Research Letters*, *40*, 1594–1599. https://doi.org/10.1002/grl.50342

Sauzède, R., Bittig, H. C., Claustre, H., Pasqueron de Fommervault, O., Gattuso, J.-P., Legendre, L., & Johnson, K. S. (2017). Estimates of water-column nutrient concentrations and carbonate system parameters in the global ocean: A novel approach based on neural networks. *Frontiers in Marine Science*, *4*, 128.

Schlitzer, R. (2004). Export production in the equatorial and North Pacific derived from dissolved oxygen, nutrient and carbon data. *Journal of Oceanography*, *60*(1), 53–62. https://doi.org/10.1023/B:JOCE.0000038318.38916.e6

Siegenthaler, U., & Sarmiento, J. L. (1993). Atmospheric carbon dioxide and the ocean. *Nature*, *365*(6442), 119–125. https://doi.org/10.1038/365119a0

Sundquist, E. T. (1985). Geological perspectives on carbon dioxide and the carbon cycle. In *The carbon cycle and atmospheric CO_2: Natural variations Archean to present*. Washington, DC: American Geophysical Union (AGU).

Takahashi, T., Sutherland, S. C., Sweeney, C., Poisson, A., Metzl, N., Tilbrook, B., et al. (2002). Global sea-air CO_2 flux based on climatological surface ocean pCO_2, and seasonal biological and temperature effects. *Deep-Sea Research Part Ii-Topical Studies in Oceanography*, *49*(9), 1601–1622. https://doi.org/10.1016/S0967-0645(02)00003-6

Talley, L. D., Feely, R. A., Sloyan, B. M., Wanninkhof, R., Baringer, M. O., Bullister, J. L., et al. (2016). Changes in ocean heat, carbon content, and ventilation: A review of the first decade of GO-SHIP global repeat hydrography. *Annual Review of Marine Science*, *8*(1), 185–215. https://doi.org/10.1146/annurev-marine-052915-100829

Talley, L. D., Pickard, G. L., Emery, W. J., & Swift, J. H. (2011). *Descriptive physical oceanography*. Cambridge: Elsevier.

van Heuven, S., Pierrot, D., Rae, J. W. B., Lewis, E., & Wallace, D. W. R. (2011). MATLAB program developed for CO_2 system calculations. ORNL/CDIAC-105b. Carbon Dioxide Information Analysis Center, Oak Ridge National Laboratory, U.S. Department of Energy

Verdy, A., & Mazloff, M. R. (2017). A data assimilating model for estimating Southern Ocean biogeochemistry. *Journal of Geophysical Research: Oceans*, *122*, 6968–6988. https://doi.org/10.1002/2016JC012650

Weiss, R. F. (1974). Carbon dioxide in water and seawater: The solubility of a non-ideal gas. *Marine Chemistry*, *2*(3), 203–215. https://doi.org/10.1016/0304-4203(74)90015-2

Whalen, C. B., Talley, L. D., & MacKinnon, J. A. (2012). Spatial and temporal variability of global ocean mixing inferred from Argo profiles. *Geophysical Research Letters*, *39*, L18612. https://doi.org/10.1029/2012GL053196

Williams, N. L., Juranek, L. W., Feely, R. A., Johnson, K. S., Sarmiento, J. L., Talley, L. D., et al. (2017). Calculating surface ocean pCO_2 from biogeochemical Argo floats equipped with pH: An uncertainty analysis. *Global Biogeochemical Cycles*, *31*, 591–604. https://doi.org/10.1002/2016GB005541

Wu, Y., Hain, M. P., Humphreys, M. P., Hartman, S., & Tyrrell, T. (2019). What drives the latitudinal gradient in open-ocean surface dissolved inorganic carbon concentration? *Biogeosciences*, *16*(13), 2661–2681. https://doi.org/10.5194/bg-16-2661-2019